ROCKET MEASUREMENTS OF PRECIPITATING ELECTRONS IN A SYSTEM OF MULTIPLE AURORAL ARCS

A

DISSERTATION

Presented to the Faculty of the

University of Alaska in Partial Fulfillment

of the Requirements

for the Degree of

DOCTOR OF PHILOSOPHY

by

John Stuart Boyd B. Sc., B. E., M. S.

Fairbanks, Alaska

August 1973

ROCKET MEASUREMENTS OF PRECIPITATING ELECTRONS

IN A SYSTEM OF MULTIPLE AURORAL ARCS

RECOMMENDED:

Chairman, Advisory Committee

APPROVED:

Director, Geophysical Institute

31 October 73
Date

Vice President for Research

1 Nov. 73
Date

ABSTRACT

The pitch angle distributions of precipitating electrons with energies 2.5, 5 and 10 kev were measured by rocket-borne detectors in a system of multiple auroral arcs. A second 10 kev detector was carried on a separating forward section of the payload. Comparison of the data from the two sections showed strong spatial variations in the electron intensity, and a detailed correspondence was found between these variations and visible auroral forms. Overall variations in pitch angle distributions and the occurrence of peaked spectra in the bright arcs were consistent with previous observations. The observation of a peaked spectrum in the background aurora was unusual. The absence of an upper cutoff in the pitch angle distribution implies that low altitude parallel electric fields were not important in the acceleration of the electrons. Rather, the detailed structure of the pitch angle distribution shows that wave particle interactions must be responsible for the field-aligned intensities in bright auroral arcs.

ACKNOWLEDGEMENTS

It is a pleasure to gratefully acknowledge the guidance and assistance in the preparation of this thesis of the members of my Advisory Committee, Prof. Vladimir Degen, Prof. John Murray, Prof. Gerald Romick and particularly, the Chairman of the committee, Dr. T. Neil Davis. I am also grateful for the atmosphere of scientific endeavor which prevails at the Geophysical Institute and for the stimulating discussions with staff members over the past six years. In particular, I would like to mention Professors A. E. Belon, R. Parthasarathy, H. R. Anderson (on leave from Rice University) and fellow graduate students, Don Wallis and Brenton Watkins, as well as Dr. Alan Johnstone, later a Post-Doctoral Fellow at NASA/Goddard Space Flight Center, Greenbelt, Md.

On the technical side, a number of persons contributed to the success of the series of rockets of which NASA 18.17 UE was one. The assistance of the following persons or groups is gratefully acknowledged. The engineering and technical staff at the Sounding Rocket Branch and other facilities at Goddard; the personnel associated with the Geophysical Institute Rocket Launching Facility, under the direction of Mr. Neal Brown; Miss Irene Soos who designed most of the on-board electronic circuitry; Mr. Gunter Hampel, payload engineer; Mr. Lou Baim, who constructed most of the mechanical and electronic systems associated with the particle detectors; Mr. Russ Wertz, who shared the scientific responsibility for this particular payload and Dr. Alan D. Johnstone, who designed the particle detectors and payloads in the series. In addition, he carried out the digitization

of the particle data from payload 18.17 while a Post-Doctoral Fellow at Goddard.

Finally, I am especially grateful to Miss Judith Holland, both for her painstaking work in typing and for her assistance in the overall editing of this thesis.

The rocket work performed here was supported by National Aeronautics and Space Administration Contracts NSR-02-001-025, NGR-02-001-082 and NGR-02-001-087.

Ground observations were supported by National Aeronautics and Space Administration Contract NAS 6-1932 and by Atmospheric Sciences Section, National Science Foundation Grant GA-32521.

TABLE OF CONTENTS

FIGURE CAPTIONS

Fig. 1.1 Idealized representation of the cross section of the magnetosphere in the noon-midnight meridian plane, showing the principal features of the particle distribution and magnetic field configuration (from Ness, 1969).

Fig. 1.2 Equivalent current system for an intense polar magnetic substorm derived from ground-level perturbations in the earth's magnetic field. Note the eastward current in the evening sector corresponding to an increase in the horizontal component (from Akasofu et al., 1965).

Fig. 2.1 A sketch of the layout of the particle detector. High voltage components are encapsulated in the central well and the amplifier is mounted over the top of the channel multiplier. Wiring connections have been omitted for clarification (Johnstone, 1970).

Fig. 2.2 Experimental response curve of the detector to an electron beam of fixed current and varying energy at normal incidence. The contribution from scattered particles is indicated. (Johnstone, 1970).

Fig. 2.3 A section of the original telemetry record photographically reproduced. The channels shown are, from bottom to top: rear section transverse magnetometer, 2.5 kev, 5 kev and 10 kev electron data; forward section 10 kev electron data. NASA 36 bit time code on a 1 kHz carrier is shown at the top and bottom of the chart. The internally generated pulse calibration sequence in the rear section data channels begins at 0818:22.181 UT.

Fig. 2.4 3 component magnetograms from College and Fort Yukon for periods around the time of launch (T = 0), which is indicated by the vertical dashed lines.

Fig. 2.5 H component magnetograms from several auroral zone stations near the time of the rocket flight. The time of launch (T = 0) is indicated by the vertical dashed line.

Fig. 2.6 All-sky photographs from Fort Yukon and Poker Flat, and scanning photometer traces in Hβ, λ4278 and λ6300 from Fort Yukon at the time of launch of the rocket.

Fig. 3.1 Illustrating the relationship between the magnetic field B, the coning axis C and the spin axis S.

Fig. 3.2 Illustrating the relationship between the magnetic field vector B, the spin axis S and the detector axis D.

Fig. 3.3 Three digitized data records for the three fixed-energy channels in the rear section of the payload with the computed pitch angle. The modulation in intensity due to the rocket spin motion is evident. Each record is almost exactly of one second duration. There are 300 data points per channel per record.

Fig. 3.4 Digitized data record for the 10 kev channel on the forward section. The time covered is approximately the same as in Fig. 3.3. The record length is 3 seconds and there are 900 data points per record. The electron data has been smoothed by taking averages of 3 points. The effect of coning is evident in addition to the spin modulation.

Fig. 3.5 Illustrating the two extreme cases of the relative orientations of the spin axis S and the magnetic field vector B. In case (a) the pitch angle coverage during a spin cycle will

be a maximum; in case (b) it will be a minimum.

Fig. 3.6 One-second average electron data from the three fixed-energy channels on the rear section and the 10 kev channel on the forward section, together with parameters derived from this data. The spectral index indicates relative "hardness" of the spectrum on a scale 0 through 5. The anisotropy ratio J(35)/J(85) is the ratio of the intensity in the pitch angle interval 32^{o} - 40^{o} to that in the interval 80^{o} - 90^{o}, averaged over each record. The visible aurora record indicates the times that either discrete or diffuse aurora were visible at the location of the rocket. The precipitated energy is simply the sum of the energy flux measured by the 3 rear section detectors over each one second record.

Fig. 3.7 Representative spectra from various points of the trajectory illustrating spectral indices, 2, 3, 4, 5 and showing the spectrum at the point of greatest energy flux at T = 247. For comparison a Maxwellian spectrum with kT = 10 kev is also plotted.

Fig. 3.8 Scanning photometer traces at T = 247 from Ester Dome Observatory (EDO) and Fort Yukon (FYU) showing the measured intensity as a function of zenith angle in λ4278.

Fig. 3.9 Relationship between the visible auroral forms as recorded by the Fort Yukon all-sky camera and the rocket trajectory at T = 247. The auroral arcs were mapped onto a horizontal plane assuming a lower border height of 110 km. The position of the rocket, mapped down the field line to that altitude is shown by a cross.

CHAPTER 1

INTRODUCTION AND REVIEW

1.1 Goals of the Thesis

An understanding of the processes responsible for the energization and precipitation of auroral particles is now the most critical task in our overall knowledge of magnetospheric dynamics. Measurement of the pitch angle and energy distributions of these particles is a powerful tool in investigating the precipitation mechanisms. While these distributions have been extensively documented by satellite and rocket-borne measurement, the measurements so far have not allowed any particular acceleration mechanism or source region to be uniquely determined.

After the early, exploratory flights which determined the general nature of the particles involved as being electrons and protons with energies in the 0.1 kev to 100 kev range, most investigators concentrated on the measurement of energy spectra. It was thought that a comparison with similar measurements elsewhere in the magnetosphere or with theoretical models, would provide insight into the source region of the particles in the magnetosphere and the processes resulting in their deposition into the atmosphere.

Coincidentally, the data obtained on several early rocket flights showed that the intensity of the precipitating particles, particularly electrons, was often highly anisotropic. It then became apparent that the pitch angle distribution was in general more indicative of the precipitation mechanism than the energy spectrum. More recently, several rocket flights have exploited the pitch angle coverage

provided by a spinning rocket to obtain simultaneous energy and pitch angle distributions.

In order to completely specify these parameters, the detectors should be capable of simultaneously measuring the pitch angle with a resolution of perhaps 10^{o} over the range 0 - 180^{o}, the energy spectrum with a resolution of a few percent, all with a spatial resolution of $\sim$ 100 m or less. Unfortunately, practical considerations of payload size, weight and available telemetry bandwidth provide a limitation below these ideal requirements. Using the spin of the rocket to provide pitch angle coverage limits the spatial resolution to the horizontal distance covered by the rocket in one spin period. Thus a fairly high spin frequency is required. However, it is then impossible to use a swept energy analyzer to obtain the energy spectrum as a function of pitch angle over a spin period because of the impossibly high telemetry bandwidth required. Also, the particle intensities may be too low to provide a significant count rate at the detector unless the area and acceptance solid angle of the detector become very large.

A compromise can be made by including perhaps one or two arrays of fixed energy detectors with their acceptance solid angle centered at some angle to the spin axis of the rocket. This angle depends on the trajectory and attitude of the rocket which are usually determined by other considerations. One of these considerations is the type of observation that is required. For instance it may be desired to investigate the particle distribution across a broad region containing several different auroral forms. The trajectory would then

be set lower and longer than it might be for other purposes in which case the spin axis makes a relatively large angle with the earth's magnetic field vector. The detector axes are then set to provide the maximum pitch angle coverage possible.

In order to use the results of these measurements to increase our understanding of the dynamics of the magnetosphere, such a rocket flight must be launched into a well-defined auroral situation. To provide this definition, two types of ground-based observations are required. The first is real-time magnetic, photometric and visual information which is coupled with the experience of the observer to determine the appropriate time to launch the rocket. Such data, obtained from stations near the trajectory are then used to accurately determine the nature of the aurora in the trajectory. The second type of observation is provided by stations around the world, and consists principally of magnetic data. These data are used to describe the overall state of the variable magnetosphere at the time of the measurements.

Once the data are obtained they can be analyzed to give descriptive information that defines the characteristics of the particle energy and pitch angle distributions and the relationship of these distributions to morphological characteristics of the aurora. In itself the aurora is one of the best means to determine the state of the local environment where the measurements are made and also the overall magnetosphere environment if adequate observations are available.

The real aim here, however, is to utilize the observations to

try to identify specific acceleration mechanisms. To assist in this effort it is desirable to bring in such other rocket observations obtained at comparable locations and at times when the local and magnetospheric environments are similar. The ability to do this depends in part upon the extent to which one can determine the environment at the time and location of each rocket flight.

The preceding statements are intended to convey the thrust of this thesis and to indicate, in broad outline, the rationale behind the various steps leading to the final goal: acquisition of new knowledge about acceleration mechanisms. Before going on to describe the observations and their interpretation it is well to briefly review the state of current knowledge about particle distributions in the magnetosphere and the more important dynamical variations they undergo.

1.2 Brief Review of Particle Distribution in the Magnetosphere

The topology of the magnetic field and the distribution of charged particles in it has been the subject of an enormous study over the last several years. A fairly consistent picture of the average structure of the magnetosphere has emerged; some of the main features of the noon-midnight section are illustrated in Fig. 1.1, taken from Ness (1969).

At the lowest magnetic latitudes is the region of stably trapped particles - the radiation belts. To a first approximation, the magnetic field lines here are dipole-like. The motions of particles trapped on these field lines are adiabatic, and the particle trapped lifetime is greater than the time taken to make one complete revolution of

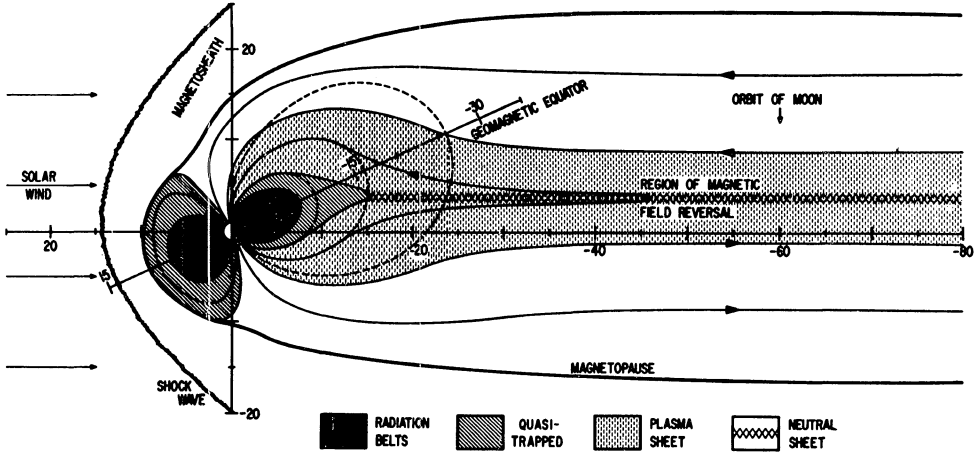

Fig. 1.1 Idealized representation of the cross section of the magnetosphere in the noon-midnight meridian plane, showing the principal features of the particle distribution and magnetic field configuration (from Ness, 1969).

the earth under the influence of the gradient and curvature drifts. The high-latitude cutoff of > 40 kev electrons routinely observed by satellites and referred to as the "trapping boundary" (e.g., Frank, 1971) is often assumed to correspond to the limit of this region of stable trapping.

At higher latitudes, but still on closed field lines is a region of "quasi-trapped" particles, which are unable to execute a complete longitudinal drift motion.

The particle population in the region of more-or-less stable trapping has been described in various terms. The "inner and outer radiation belts" (Van allen et al., 1959) describe regions of apparently stably trapped energetic particles, concentrated in two regions. In the inner region between L = 1 and L = 3, the energy is carried mainly by electrons with energy $\sim$ 1 Mev. The stability of these particles has been demonstrated by the length of time required for the decay of energetic particles injected into the region by high altitude nuclear explosions (McCormac, 1966; several papers). This population of energetic electrons is apparently not important in the understanding of aurorally related processes.

In the same region there is a relatively dense, very low energy plasma (1 $\sim$ 500 ev) known as the plasmasphere. Under quiet conditions, it may extend out to L $\sim$ 6, and its boundary is usually well defined as a decrease in the electron density of up to 10^3 over a range of increasing L of a few tenths. (Russell and Thorne, 1970; Carpenter, 1966). The plasmasphere has been the subject of considerable interest, particularly in relation to the formation of stable auroral

red (SAR) arcs, and studies of VLF propagation and related effects (Carpenter et al., 1972). It is thought that the outer boundary of the plasmasphere, the plasmapause, is at least related to the boundary between the region where the plasma motion is dominated by co-rotation, and that where convective motion induced by a magnetospheric electric field is dominant (Brice, 1967).

In the outer region, at least 75% of the energy is carried by protons with energy of a few tens of kev. Much of our knowledge of the average properties of this region comes from observations on OGO 3 (Schield and Frank, 1970; Owens and Frank, 1968; Frank and Owens, 1970; Frank, 1970, 1971). These protons are found over a range of L from L $\sim$ 5 to L $\sim$ > 10 during magnetically quiet periods, with a half intensity width $\sim$ 1 L shell centered at L $\sim$ 6. The spectrum in this region shows a broad peak from $\sim$ 10 to > 30 kev, and the peak omnidirectional intensity is $\sim 10^7$ cm^{-2} sec^{-1} kev^{-1}.

Electrons in the same region show a spectrum with a broad peak between $\sim$ 1 and $\sim$ 10 kev and peak intensities of $\sim 10^8$ cm^{-2} sec^{-1} kev^{-1} (Schield and Frank, 1970). Frank (1971) has shown that the energy density is a function of L value and magnetic activity and the ratio of the proton energy density to the electron energy density is highly variable over the range 2 to 40.

There are some convincing arguments that the inner edge of the ring current proton population is controlled by the plasmapause. Briefly, the likely mechanism is that the presence of the low energy plasma at the plasmapause destabilizes proton cyclotron waves as the energetic proton population is moved into the plasmapause region

by convection (Cornwall, et al., 1970, 1971). The ion cyclotron waves, whose growth is greatest near the equatorial plane, propagate along the field lines and undergo Landau damping by almost-resonant electrons in the topside ionosphere. The result is that the electron temperature is raised to $\sim 10^4$ ^oK, so that at least the electrons in the high energy tail have sufficient energy to excite the λ6300 (OI) emission. This mechanism explains the usual spectral purity of the SAR arcs and is supported by simultaneous observations of plasmapause, ring current and SAR arcs reported by Chappell et al., (1971). The location of the plasmapause is related to overall magnetic storm activity, as measured by Kp or Dst indices. Under quiet to moderately disturbed conditions, it appears in the range L = 6 to L = 3.

The behavior of the ring current proton distribution is not so clear, however. The OGO 3 data show distributions under various conditions of magnetic activity. (Frank, 1970; Frank and Owens, 1970). It is not possible from these data to infer the behavior of the ring current proton distribution with substorm activity, although Frank et al., seem to imply that the location of the peak in the proton population does exhibit substorm related behavior.

On the other hand, if it is possible to identify this peak with the region of precipitated protons as identified from the ground by neutral hydrogen emissions produced as a result of charge exchange reactions, then the behavior is well documented. Eather and Carovillano (1971) argue that the region of the peak proton intensity is the source of the proton aurora. The behavior of the hydrogen emission

region has been extensively documented (Rees et al., 1961; Montbriand, 1971).

On the assumption that the proton aurora does map the peak proton intensity, it follows that the energetic proton distribution behaves in a substorm related manner. Briefly, the proton region shows a diurnal behavior consistent with convective motion (Taylor and Hones, 1965). To an observer at auroral latitudes, this is manifested as an equatorward movement of the proton aurora in the early evening hours, so that it is a few degrees of latitude equatorward of the quiet electron produced auroral arcs. At the time of onset of the expansive phase of a substorm defined by the auroral breakup, the proton precipitation region becomes as widespread and difficult to document as the electron precipitation region. It appears to expand both north and south. However, in a fairly quiet situation, that is, when a substorm occurs in the midnight sector and is isolated in space and time, the proton precipitation region seems to reform and resume its diurnal behavior apparently dominated by the convection processes. This behavior of the proton region is in contrast to the behavior of the plasmapause as indicated by the morphology of the SAR arc which remains at a relatively constant location during the expansion and other movement of the hydrogen emission region and hence presumably, the proton ring current (Hoch et al., 1971). However, the morphology is not entirely clear.

Moving outward in the magnetosphere, the next region of interest is the plasma sheet. This is a region of medium energy plasma (1 $\sim$ 10 kev) which extends from somewhere in the ring current proton distribution

out into the tail region. The inner edge is defined by Frank (1971) as an exponential decrease in the electron energy density with decreasing L value. The number density remains fairly constant. The plasma sheet is sometimes divided into two components: the "near earth plasma sheet" and the "distant plasma sheet". The near earth plasma sheet can be defined by the region of more dipole-like field lines, and extends to perhaps 10 R_E. Beyond that distance the field lines are definitely non-dipole-like and a neutral sheet current exists to maintain the configuration. It is thought by many that the auroral arcs forming the quiet auroral oval are produced by electrons precipitated from the plasma sheet as they are convected inwards by the magnetospheric electric field. (Vasyliunas, 1968).

Models such as that of Taylor and Hones (1965) have been solved for the adiabatic motion of electrons and protons originating at the boundary of a closed magnetosphere. In the Taylor and Hones model the electric field is derived from an equivalent current system representing the global magnetic disturbance of a moderate magnetic storm, and the contours of equal horizontal sheet current density were assumed to be electric equipotentials. While this and other assumptions made are not necessarily accurate, the general features of particle precipitation patterns predicted by the model agree at least qualitatively with the observed behavior of quiet auroral arcs (Boyd et al., 1971). The convection process proceeds until the loss rate due to the pitch angle diffusion of particles into the loss cone equals the cross L diffusion due to the convection (Kennel and Petschek, 1966). The result is a plasma sheet distribution with

a fairly well-defined inside edge (Schield and Frank, 1970; Frank, 1971).

1.3 The Magnetospheric Substorm

The end of the quiet convective phase described in the previous section is usually marked by a sudden increase in magnetic activity at auroral latitudes, accompanied by rapid increases in the brightness, extent and activity of the previously quiet auroral arcs. Also, micropulsation and other activity increases, and it is apparent that processes dramatically different from the quiet convection described earlier are occurring.

The mechanism which triggers and maintains this substorm, as it is called, is not understood. It is known that usually several things happen, some almost simultaneously. These include: a sudden increase in the reconnection rate of field lines in the tail, a thinning or depletion of the plasma sheet in the tail at $\sim 18\ R_E$, and presumably the onset of large scale plasma instabilities which produce the intense, widespread and active aurora, as well as other effects. The onset of the rapid increase in auroral activity is usually referred to as the auroral breakup. The horizontal magnetic perturbations observed during a substorm can be represented by an equivalent horizontal current system in the ionosphere. Figure 1.2 shows such a system derived for an intense substorm (Akasofu et al., 1965). Extensive review of the magnetic and other effects of substorms have been given (e.g., Akasofu, 1968), and no attempt at a detailed review will be made here.

A typical substorm may cause perhaps 10^{21} ergs to be dumped

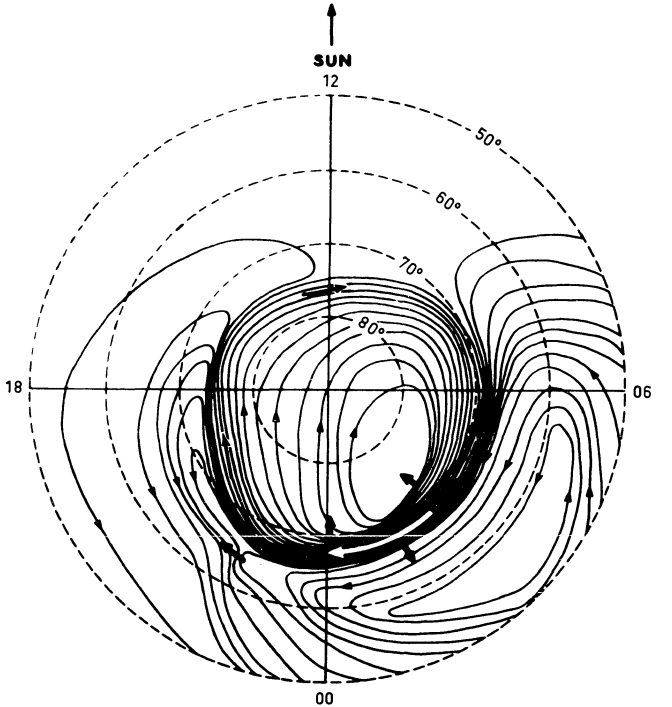

Fig. 1.2 Equivalent current system for an intense polar magnetic substorm derived from ground-level perturbations in the earth's magnetic field. Note the eastward current in the evening sector corresponding to an increase in the horizontal component (from Akasofu et al., 1965).

into the atmosphere (Akasofu, 1968), this energy being carried as the kinetic energy of precipitated particles. It was thought that there was ample energy stored in the ring current energetic proton distribution, and the high energy electron (> 40 kev) population to account for the substorm. However, beginning with O'Brien (1963) observations indicate that this is not the case. It now appears that the substorm is the mechanism by which the ring current proton population is increased (Davis and Parthasarathy, 1967; Davis, 1969). That is, during the substorm, particles are rapidly transported in to low L values, some precipitating, but a number, greater by a factor of 10^2 or more, forming an enhanced trapped population.

Swift (1967) suggested that the auroral breakup is caused by an interchange instability occurring on the outer boundary of the ring current proton distribution. The criterion for instability is that the plasma density gradient be sufficiently high. Hasagawa (1971) doubts that the gradient can, in fact, become high enough. Another difficulty is that satellite and other observations suggest that the proton ring current moves inwards, i.e., to lower latitudes during substorms, whereas the breakup aurora expands polewards. Also, the breakup occurs at too high a latitude, during storms, to be associated with the ring current which has moved in to $L \sim 3$.

There is another difficulty with this model, in that, as mentioned earlier, it appears that the ring current increases in intensity during a substorm, and frequently remains more intense after than before the substorm (Davis, 1969). This does not say that the density gradients are steeper after the substorm than before, but it seems

reasonable to assume that they would be comparable, and therefore unstable at a time when they are observed to be stable.

Recent analysis of observations (Johnstone et al., 1973) suggests that the breakup intiates near the inner edge of the plasma sheet. Assume that an interchange instability initiated in this region, due at least in part to the plasma density gradient. Then such a process would "eat away" at the inner edge of the plasma sheet, moving the interaction region further from the earth as it proceeds. This corresponds to a poleward movement of the region of precipitation, which is more in agreement with observations.

Convection models with a static magnetic field configuration have been unable to account for the rapid penetration of particles and energy during the substorm. The only reasonable source of the energy appears to be the extended tail region. Observations indicate that at the onset of a substorm, the plasma sheet at 18 R_E in the tail thins (Hones et al., 1971a) and the magnetic field vector becomes more dipole-like. This suggests that reconnection is occurring in the tail, and the newly merged field lines then contract towards a dipole configuration thereby converting magnetic energy into particle energy through the Fermi-betatron process. The onset of Pi micropulsations at the breakup has been attributed to these inward propagating field lines (Axford, 1969). Sharber and Heikkila (1972) attribute the overall increase in particle energy observed during substorms to Fermi acceleration along contracting field lines.

This brief discussion of the particle distribution and dynamics of the magnetosphere is intended to provide a broad framework in

which to place the observations and discussions which follow. While the main aim is to investigate auroral particle precipitation mechanisms, it is important to relate results to the dynamic state of the magnetosphere in order to further the overall aim of understanding the dynamics of the magnetospheric system.

CHAPTER 2

NIKE-TOMAHAWK NASA 18.17 UE FLIGHT DATA

2.1 The Purpose of the Flight

The main data on which this thesis is based was obtained by electron detectors carried on a Nike-Tomahawk rocket, NASA 18.17 UE, launched from Poker Flat, Alaska at 0815:16 UT on 20 March 1971. NASA 18.17 UE was one of a series of five (18.13 through 18.17) Nike-Tomahawks carrying payloads designed to investigate auroral particle precipitation mechanisms, auroral electrojet activity and their relationship to the dynamics of the magnetosphere. Results obtained from other rockets in the series are given by Johnstone (1970, 1971), Johnstone and Davis (1973) and Johnstone et al. (1973).

The principal parameters to be measured aboard rocket 18.17 were the energy and pitch angle distributions of precipitating particles, particularly electrons, and perturbations in the magnitude of the geomagnetic field due to auroral electrojet currents.

In order to be able to interpret these measurements in terms of particle transport and precipitation mechanisms in the magnetosphere, it was necessary that the rocket be launched into an auroral situation in which the auroral processes were expected to be significant in the development of the magnetospheric substorm.

On the basis of previous observations, it was decided to launch the rocket into one or more relatively stable auroral arcs, at a time that ground-based magnetometers indicated the existence of an east-west electrojet in the vicinity of the arcs. An additional condition was that the behavior of the aurora indicate that an increase in activity, in particular, an auroral breakup, was imminent.

2.2 Instrumentation

The payload consisted of two separating sections. The forward section contained a rubidium vapor magnetometer and two fixed energy electron detectors. It was constructed as far as possible of fiber glass, with a ceramic nose cone, and the magnetometer sensor was mounted in a fiberglass holder inside the nose cone. The electronic components of the magnetometer were constructed of non-magnetic materials, as were the components of the electron detectors and the telemetry system. The aim was to reduce the magnetic field due to the payload to $< 1\gamma$ at the sensor.

The rear section contained four electron and two proton detectors, two photometers, and two fluxgate magnetometers to determine the aspect of the vehicle relative to the earth's magnetic field. A monitor device was included to confirm the separation of the payload which was accomplished by compressed springs released by an explosive pin.

The performance of these detectors is summarized in Table 2.1.

2.3 Particle Detectors

The particle detectors each consisted of a 90^{o} cylindrical electrostatic analyser, with a Bendix continuous channel electron multiplier (channeltron) as the detecting element. The design of the device has been described previously (Johnstone, 1970). A simplified drawing is shown in Fig. 2.1. The proton detectors were modified on Payload 18.17 by increasing the separation of the analyser plates. This produced a greater energy bandwidth, and thus an increased count rate.

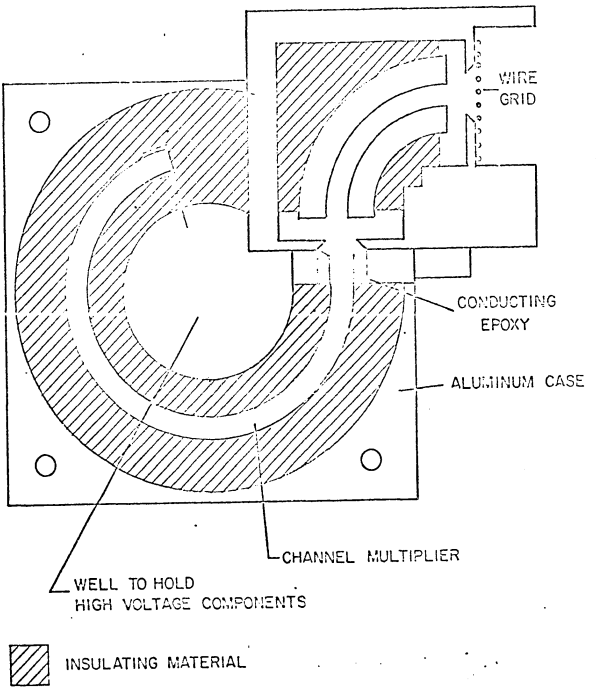

Fig. 2.1 A sketch of the layout of the particle detector. High voltage components are encapsulated in the central well and the amplifier is mounted over the top of the channel multiplier. Wiring connections have been omitted for clarification (Johnstone, 1970).

TABLE 2.1

SUMMARY OF INSTRUMENT PERFORMANCE ON

NASA 18.17 UE

INSTRUMENT		CONDITION OF DATA
Rear Section		
Electron detectors	2.5 kev	Satisfactory
	5 kev	Satisfactory
	10 kev	Satisfactory
Swept Energy		No Data
Proton Detectors	2.5 kev	No Data
Swept Energy		No Data
Hβ photometer		No Data
λ5577 photometer		No Data
Aspect magnetometers		Satisfactory
Forward Section		
Electron detectors	5 kev	failed 15 seconds after turn on.
	10 kev	Satisfactory
Rb vapor magnetometer		fair; severely affected by coning.
Separation monitor		confirmed separation of T = 50 sec with a separation speed ~ 2.0 msec^{-1}

A characteristic of the cylindrical electrostatic analyser is that the bandwidth is proportional to the center energy of the pass-band, E_o. The electron detectors were calibrated using an electron beam of constant current vertically incident on the entrance aperture. With the electron acceleration voltage held constant, the analyzer plate voltage was swept to determine the energy bandwidth. The peak response of the three fixed-energy detectors agreed within 10%. A typical response curve is shown in Fig. 2.2. The bandwidth of the electron detectors on 18.17 was 0.23 E_o. The geometric factor for the electron detectors has been calculated by Johnstone (1970) as 1.5×10^4 E_o cm^2 ster kev.

The count rate of the detectors is also affected by the variation of the counting efficiency of the channeltrons with the energy of the incident electrons. Results of measurements of this efficiency vary, but the ratios between the values at different energies are fairly consistent. The values used by Johnstone (1970) were adopted, and the overall conversion constants for the detectors were determined as shown in Table 2.2. This is the factor by which the count rate (sec^{-1}) must be multiplied to give the measured intensity in cm^{-2} sec^{-1} kev^{-1} $ster^{-1}$.

TABLE 2.2

CONVERSION FACTORS FOR ELECTRON DETECTORS

Energy (kev)	Channeltron Efficiency	Conversion Factor
2.5	0.34	0.78×10^4
5	0.25	0.53×10^4
10	0.18	0.37×10^4

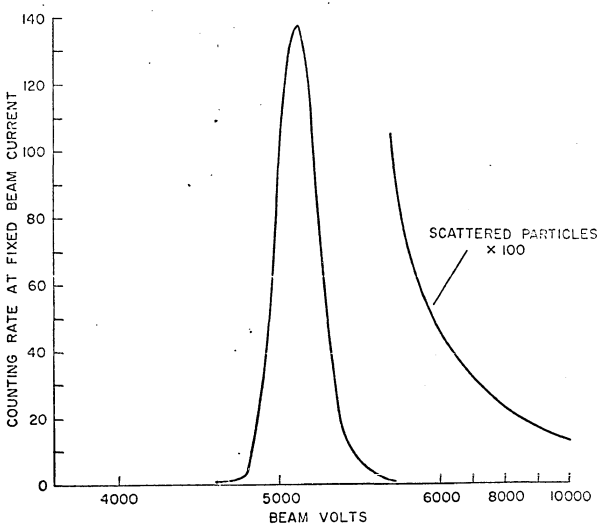

Fig. 2.2 Experimental response curve of the detector to an electron beam of fixed current and varying energy at normal incidence. The contribution from scattered particles is indicated. (Johnstone, 1970).

2.4 Telemetry System

The output of the channel multiplier in each particle detector was in the form of a pulse approximately 1 volt in amplitude. A discriminator amplifier reformed these into ∿ 3V x 1 micro second pulses suitable for digital processing. A step voltage generator was programmed to produce a discrete voltage depending on the number of pulses accumulated in a 3 millisecond period. The voltage steps, in the range 0-5 volts were set to represent integral counts of 2^n (n = 2,9) with the last step, from 256 to 512 further divided into 4 euqal steps. An internal pulse generator was switched to provide a calibration sequence approximately every minute. The output of the stepped voltage generator was used to modulate a standard IRIG subcarrier oscillator.

Figure 2.3 shows a section of a photographic record of the demodulated data from the telemetry system. The NASA 36-bit time code is visible at the top and bottom of the chart. The channels shown are the transverse aspect magnetometer and the three electron channels from the rear section, with the 10 kev electron data from the forward section at the top. The vertical lines are 0.1 sec apart. The section shown was chosen to include an internal pulse calibration sequence on the rear section detector channels. Spin modulation is apparent in the higher energy channels.

2.5 Ground Observations

Ground-based instruments operated specifically in conjunction with this rocket flight, as well as other data routinely available, are shown in Table 2.3.

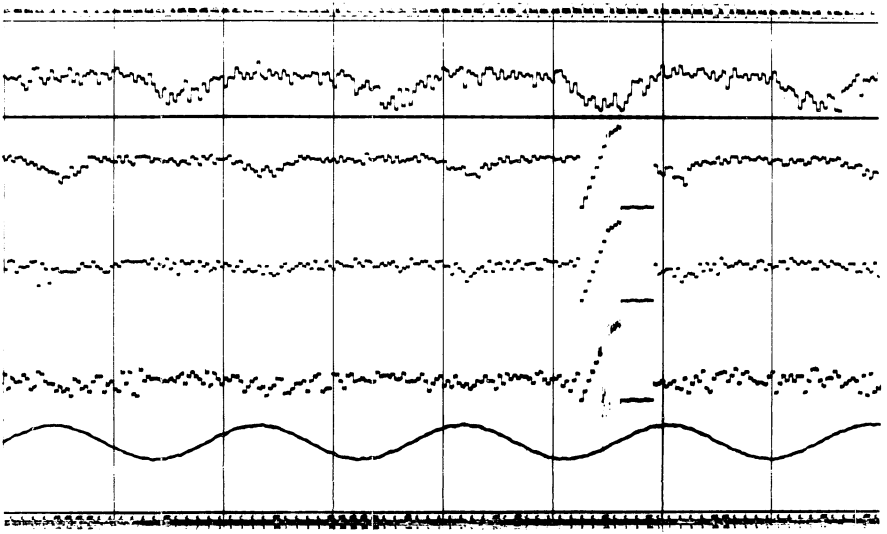

Fig. 2.3 A section of the original telemetry record photographically reproduced. The channels shown are, from bottom to top: rear section transverse magnetometer, 2.5 kev, 5 kev and 10 kev electron data; forward section 10 kev electron data. NASA 36 bit time code on a 1 kHz carrier is shown at the top and bottom of the chart. The internally generated pulse calibration sequence in the rear section data channels begins at 0818:22.181 UT.

TABLE 2.3

GROUND-BASED OBSERVATIONS AVAILABLE DURING

THE FLIGHT OF 18.17

Instrument	Stations	Remarks
4 channel scanning Photometer	EDO FYU	
Riometer	FYU COL	
Image orthicon TV	EDO FYU	Intended to track rocket flashing light
Magnetometer (3 component fluxgate)	PKR FYU	
Magnetometer (standard)	COL	Available from World-wide stations
16 mm all-sky cameras	EDO FYU	
35 mm all-sky cameras	EDO PKR FYU	
Skilled visual observers	EDO PKR FYU	

The symbols, EDO, PKR, FYU and COL refer to the Ester Dome Observatory, Poker Flat rocket launching site, Fort Yukon Observatory and College, Alaska respectively.

The four channel scanning photometers scan in the common meridian plane through EDO and FYU. The intensity at four auroral wavelengths is recorded as a function of zenith angle. The wavelengths used are λ5577 and λ6300 OI , λ4278 (N_2^+ 1 P.G.) and λ4861 (Hβ). The scan rate was variable, but was approximately one second from horizon to horizon during the flight. The field of view was circular and $\sim 1.25^o$ in diameter.

The image orthicon TV systems are capable of detecting aurora of intensity approximately equal to the visual threshold. Their primary purpose in this experiment was to track the rocket by means of two onboard lights flashing at $\sim 1\ sec^{-1}$. Incidentally the cameras record details of the aurora in the trajectory not apparent from other observations.

2.6 Rocket Performance

The rocket was launched at 0815:16 UT on 20 March 1971 on a nominal true azimuth of 30^o. The TV camera at Ester Dome, which was tracking the on-board flashing lights, showed the vehicle veer in azimuth during the burn of the Tomahawk motor and the trajectory moved out of the field of view of the camera. After the camera azimuth was adjusted, the flashing light was not detected. The NASA radar, operating at the launch site, also detected a change in azimuth, to approximately 5^o. Operating on "skin track" only, that is, relying entirely on reflection from the vehicle itself, the radar can only obtain useful data during the first 40 seconds or so of the flight. Using these data as initial conditions, a vacuum trajectory was calculated by NASA Goddard Space Flight Center which showed an

apogee of 185 km and a down-range distance at impact of 260 km, corresponding to an average horizontal speed of $\sim$ 0.64 km sec^{-1}. This trajectory was somewhat lower and longer than the anticipated trajectory, which showed an apogee of 225 km and a range of 160 km. That the apogee was lower than expected was confirmed by the data from the rubidium magnetometer.

2.7 Auroral Conditions During the Flight

The flight took place during the recovery period of a moderate magnetic storm which began with a sudden commencement at 1235 UT on 19 March 1971: Solar flare activity reached a peak on 18 March, and the whole period 12 through 20 March appears to be the third in a series of 5 fairly well defined disturbed periods recurring at intervals corresponding approximately to one solar rotation. The value of the magnetic index Kp reached a maximum of 4 on the UT day 20 March, during the period containing the rocket flight time.

Inspection of the magnetic records from College for the 24 hour period around the time of the flight (Fig. 2.4) shows that generally disturbed conditions prevailed. The H component showed a positive value from 00^h UT through to almost 11^h UT, when there was a rather abrupt decrease in activity to almost a quiet day level. This effect was world wide. The positive bay was associated with intense negative bay activity to the east. Figure 2.5 shows the H component magnetograms for several auroral zone stations to the east of Alaska. The most active station was Liervogur. Higher latitude stations - Baker Lake, Fort Churchill and Great Whale River - show less pronounced activity. The overall pattern of magnetic disturbance is consistent with the

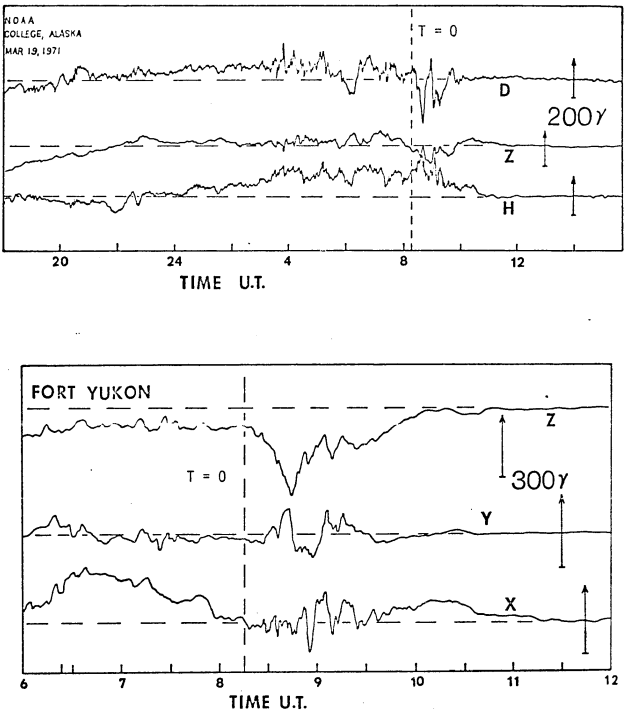

Fig. 2.4 3 component magnetograms from College and Fort Yukon for periods around the time of launch (T = 0), which is indicated by the vertical dashed lines.

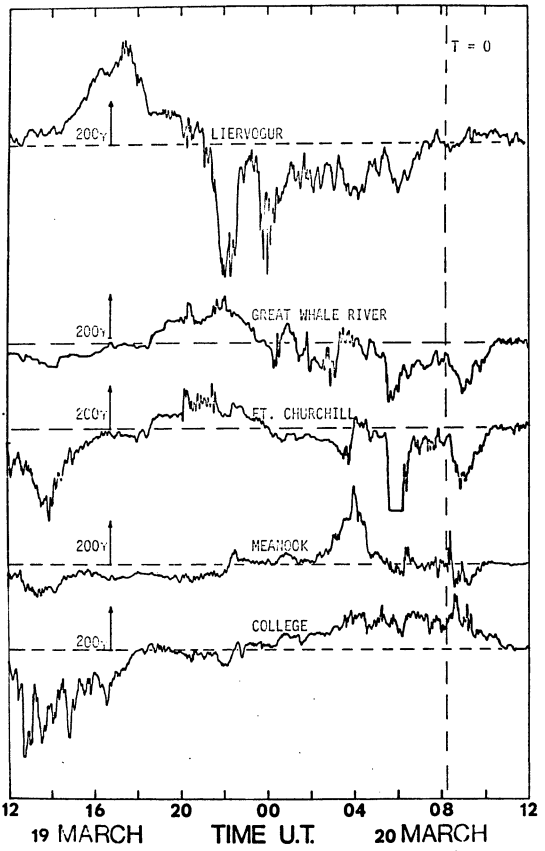

Fig. 2.5 H component magnetograms from several auroral zone stations near the time of the rocket flight. The time of launch (T = 0) is indicated by the vertical dashed line.

decay of a strong electrojet system, similar to that described by Akasofu et al., (1965) and shown in Fig. 1.2 The intensity of the disturbance peaked between 22^h and 02^h near Liervogur.

Superimposed on this global pattern are smaller scale magnetic disturbances. One of these is discernable in Fig. 2.4 at 0600, when the X component at Fort Yukon and the H component at College show small negative bays superimposed on the general positive trend. As seen by the Fort Yukon all-sky camera, an arc in the zenith brightened and moved northwards, in a manner similar to a small breakup.

Figure 2.6 shows the aurora at the time of launch as recorded at Poker Flat and Fort Yukon. The multiple arc system visible between the stations had brightened considerably beginning ∿ 0800. This brightening had, in fact, signalled a possible resumption of the countdown on the launch of the rocket. A further brightening in the east occurred just before lift-off, and this can be seen in Fig. 2.6

The meridian scanning photometer traces from Fort Yukon are also shown in Fig. 2.6 for three wavelengths - λ4278 (N_2^+), λ4861 (Hβ) and λ6300 OI.. A region of proton precipitation as measured by the Hβ emission had moved slowly southward during the few hours immediately preceding the launch, and appears well to the south of the rocket trajectory. A faint region of emission of λ4278 is apparently associated with this proton precipitation. This early evening behavior, coupled with the prevailing positive excursion in the H component seemed typical of the evening sector, and added to the visible appearance of the aurora, suggested that a breakup was imminent.

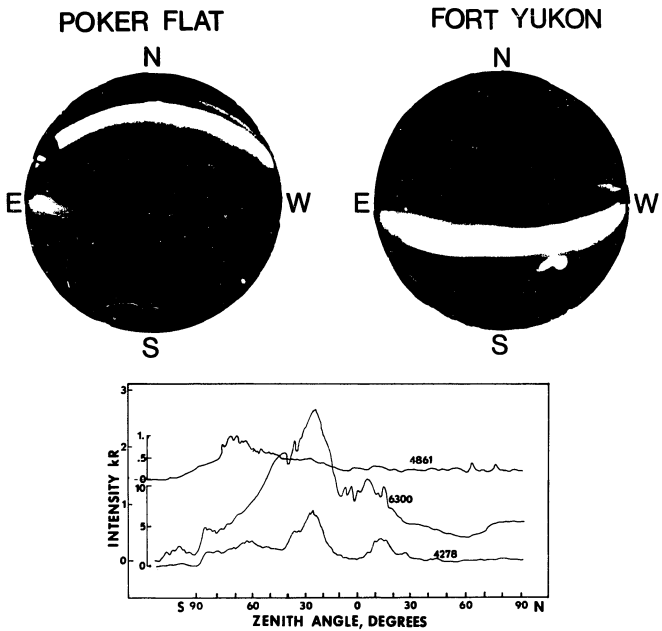

Fig. 2.6 All-sky photographs from Fort Yukon and Poker Flat, and scanning photometer traces in Hβ, λ4278 and λ6300 from Fort Yukon at the time of launch of the rocket.

However, as already discussed, the situation was much more complicated. The ratio of intensities I(6300)/I(4278) decreases with increasing characteristic energy of the incoming electrons up to a few kev. However, in this case, there is no significant change in the ratio over the region of active aurora. This suggests either that there is no change, or that the characteristic spectrum is hard enough so that a significant amount of energy is carried by electrons with energy greater than a few kev.

CHAPTER 3

REDUCTION AND INITIAL ANALYSIS OF 18.17 PARTICLE DATA

3.1 Data Digitization

As described earlier the particle data were transmitted via the telemetry system as a quasi-analog signal in which the voltage level at the discriminator output increased in discrete steps at predetermined count rates totalled over a 3-msec period. The preliminary processing of the data consisted of digitizing the signal without reference to its significance at a sampling rate of 1 kHz. The resultant output from the entire flight was then analyzed for frequency of occurrence of discrete voltage levels. Thus a histogram was constructed which showed the voltage levels in the received record which corresponded to the various integral count levels. This procedure eliminates any distortion or shift of voltage level which may have occurred. The digitized record was then reprocessed, ascribing count totals determined from the histogram analysis to the sampled voltage levels. The final result is a series of records with the initial time determined to the nearest millisecond and a series of 3-msec count totals in each of the data channels.

3.2 Vehicle Attitude Determination

As mentioned earlier, the pitch angle coverage is provided by the spinning motion of the rocket about its long axis. This spin is deliberately imparted during the acceleration through the atmosphere in order to stabilize the direction in space of the rocket axis. In order to investigate the dependence of the observed particle intensity on pitch angle, the angle between the particle detector

axes and the magnetic field must be determined as a function of time throughout the flight. This, in turn, requires an accurate determination of the vehicle attitude and spin phase.

The rear section of the payload was equipped with two fluxgate magnetometers, mounted with their axes orthogonal, and one axis parallel to the long axis of the payload. The output of each instrument is a voltage proportional to the component of the magnetic field along the positive axis of the instrument. That is, they can distinguish parallel and anti-parallel components. These magnetometers were calibrated in the magnetic calibration laboratory at NASA's Goddard Space Flight Center, Greenbelt, Maryland.

The mass distribution of the vehicle is assumed to be symmetrical about the longitudinal axis. It thus behaves as a "symmetrical top" in the absence of external torques. The rocket was spun up to $\sim$ 6 Hz. In addition to this spin about the long axis, the axis itself usually acquires a "coning" motion or force-free precession. This is caused by small asymmetries in mass distribution or non-symmetric forces occurring during the burning of the rocket motors.

To simplify the treatment, the problem is solved in two stages. In Fig. 3.1, the coning axis, C, which is the direction of the total angular momentum vector, is taken as the z axis of an orthogonal coordinate system. The magnetic field vector, $\vec{B}$, makes an angle α with the coning angle. The spin axis, $\vec{S}$, makes an angle, γ, with the coning axis, and precesses around it with an angular frequency Ω.

Defining the yz plane as that containing B and C, the angle

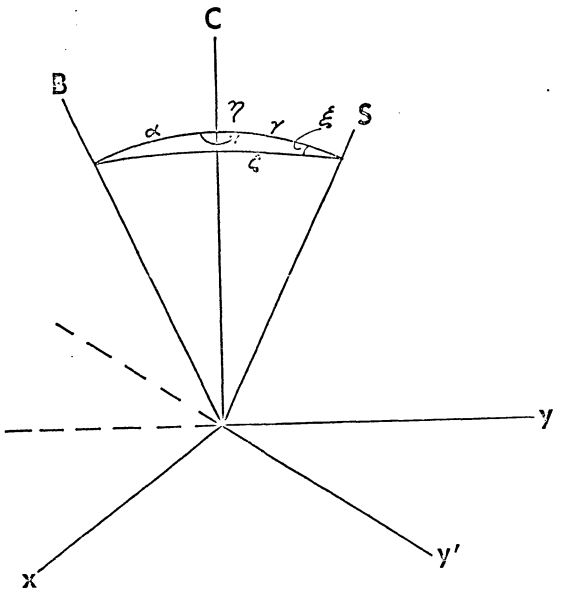

Fig. 3.1 Illustrating the relationship between the magnetic field B, the coning axis C and the spin axis S.

η is the angle between the BC plane and the CS plane,

$$\eta = \Omega t + \eta_o$$

where t is the elapsed time from some arbitrary reference point, and η_o is the value of η at t = 0.

The spherical triangle BCS can be solved to find ξ, the angle between the planes CS and BS.

$$\cos \zeta = \cos \alpha \cos \gamma + \sin \alpha \sin \gamma \cos \eta \qquad (1)$$

$$\text{and } \sin \xi = \frac{\sin \alpha \sin \eta}{\sin \xi} \qquad (2) \qquad (2)$$

Now consider a set of axes with z' along S and CS defining the y'z' plane. A second diagram, Fig. 3.2, shows the detector axis D. which makes an angle β with S and rotates around S with angular frequency ω measured relative to the y' axis. Angle ϕ is the angle between the y'z' plane and the SD plane, and is given by

$$\phi = \omega t + \phi_o$$

where ϕ_o is the value of ϕ at t = 0.

The angle between the BS and SD planes is

$$\Psi = \phi - \xi$$

Solving the spherical triangle BSD

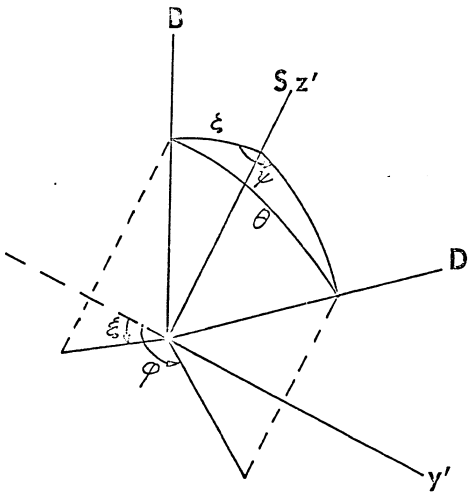

Fig. 3.2 Illustrating the relationship between the magnetic field vector B, the spin axis S and the detector axis D.

$$\cos\Theta = \cos\zeta\cos\beta + \sin\zeta\sin\beta\cos\Psi \tag{3}$$

where Θ is the required angle between the detector axis and the magnetic field vector.

Care must be taken to maintain the correct phase relationships between ξ and Ψ against the ambiguity in solving (2) for ξ. If $\alpha > \gamma$, an examination of Fig. 3.1 shows that $\cos\xi > 0$ for $\eta_o < \eta < 2\pi - \eta_o$, where η_o is the value of η of which $\xi \to \pi/2$. For computational purposes, (3) is written

$$\cos\Theta = \cos\zeta\cos\beta + \sin\xi\sin\beta\,(\cos\phi\cos\xi\ \text{sign} - \sin\phi\sin\xi) \tag{4}$$

where sign = + 1 for $\eta_o < \eta < 2\pi - \eta_o$ and - 1 otherwise.

If $\alpha < \gamma$, $\xi > 0$ for $0 < \eta < \pi$ and $\xi < 0$ for $\pi < \eta < 2\pi$. Also, $|\xi| < \eta < \pi/2$. Equation (3) then becomes simply

$$\cos\Theta = \cos\zeta\cos\beta + \sin\zeta\sin\beta\,(\cos\phi\cos\xi - \sin\phi\sin\xi) \tag{4a}$$

In the case of the rear section of Payload 18.17 the coning angle α was small (1.9^o) compared with the field of view of the detectors. The effect of coning therefore, was neglected, that is $\alpha = \Omega = 0$, and the equation (3) reduces to

$$\cos\Theta = \cos\gamma\cos\beta + \sin\gamma\sin\beta\cos\phi \tag{5}$$

where $\phi = \omega t + \phi_o$ as before.

The angle ϕ_o depends on the angle between the two planes formed by the spin axis with the detector axis and with the transverse magnetometer axis. The values of the various constants for Payload 18.17 are as follows:

$\gamma = 33^o$

$\beta = 65^o$

$t_o = 08^h\ 17^m\ 39.644^s$ UT

$\phi_o = 105^o \qquad \omega = 33.64545$

Figure 3.3 shows an example of three consecutive data records. The spin modulation in the three electron channels is evident, and the pitch angle Θ is plotted below them. The coincidence of the minima in the count rates and the maxima in the pitch angle is evident.

The case of the forward section is much more complicated. No direct attitude data are available, and the problem must be solved indirectly. The variables to be determined are the angle α between the coning axis and the magnetic field, the angle γ between the coning axis and the spin axis, the coning frequency Ω, and the spin frequency ω, as well as their respective phases.

At first sight, it may seem possible to obtain an estimate of an upper limit of the coning angle from an analysis of the angular momentum imparted to the two sections at separation. The dynamics of each section are described as the classic case of the force-free motion of a symmetric top. (See, e.g., Marion, 1970, p. 380.) The angular momentum of each section is a constant. In the case of the rear section, both the spin frequency and the coning frequency are known. This allows the kinetic energy of the rotation about the

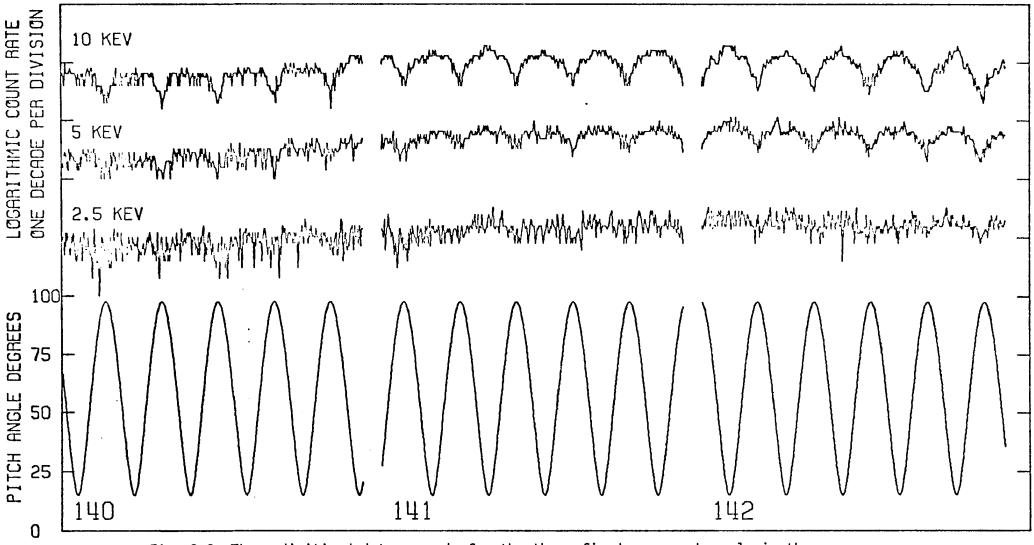

Fig. 3.3 Three digitized data records for the three fixed-energy channels in the rear section of the payload with the computed pitch angle. The modulation in intensity due to the rocket spin motion is evident. Each record is almost exactly of one second duration. There are 300 data points per channel per record.

axes orthogonal to the long axis to be calculated. Assuming that before separation the coning angle was zero, then the kinetic energy in these components will be equal for the two sections, and thus the angular momentum about the orthogonal axes may be found for the forward section. However, it is unlikely that the coning angle is zero before separation, in fact, the aspect magnetometer data indicate that it is not, and it is impossible to ascribe any particular portion of the coning effect to the separation process. Thus it is necessary to attempt an empirical solution.

It is evident from the particle and magnetic data that the coning angle α was not zero. Figure 3.4 is a typical record showing not only spin modulation of the count rate, but a longer-period modulation due to coning.

The coning period was obtained by inspection over as long a period in the data as possible. Averaged over 43 coning periods, the coning frequency was found to be

$$\Omega = 2.45658 \text{ rad sec}^{-1}$$

The time of the maximum effect of the coning motion on the spin modulation was determined for some 20 well-defined cases, and a least squares straight line fit obtained to give a zero reference point. This was then backspaced to a convenient point to give

$$\eta = \pi \text{ at } 1817{:}31.292 \text{ UT} .$$

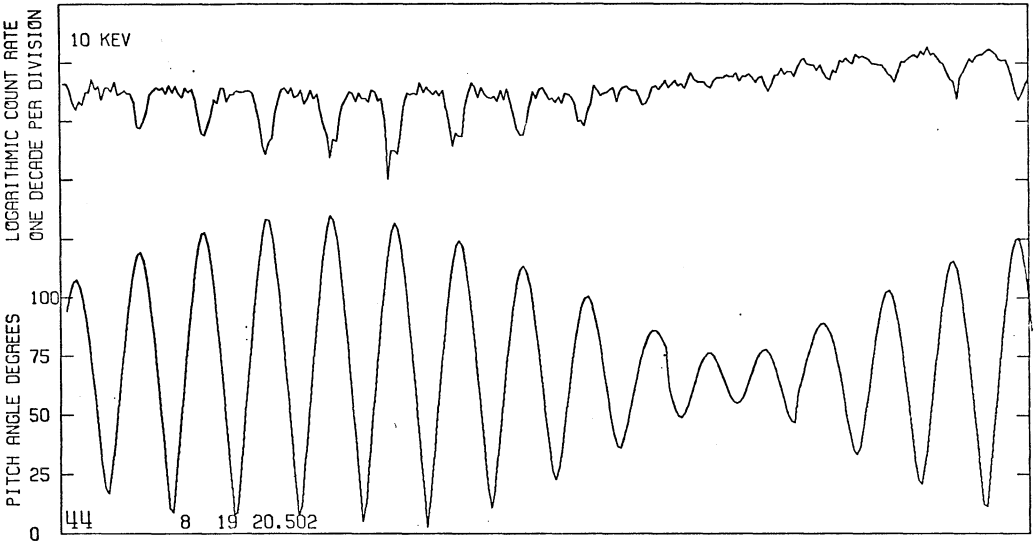

Fig. 3.4 Digitized data record for the 10 kev channel on the forward section. The time covered is approximately the same as in Fig. 3.3. The record length is 3 seconds and there are 600 data points per record. The electron data has been smoothed by taking averages of 3 points. The effect of coning is evident in addition to the spin modulation.

The apparent spin rate was found by inspection of the photographic telemetry record and averaging over 700 consecutive cycles. The apparent spin period was found to be 0.1920167 sec. Referring to Fig. 3.1 and the relevant discussion, it can be seen that if $\alpha < \gamma$, then Ψ, and therefore the spin phase, is retarded by 2π every coning period, whereas, if $\alpha < \gamma$, there is no net effect over a coning period. Which is the case cannot be immediately determined from inspection of the data.

Comparison of the 10 kev data from the two sections, as shown in Figs. 3.3 and 3.4, shows that the maximum spin modulation of the forward section data is greater than that of the rear section. This difference implies that the minimum pitch angle at a time of maximum coning effect must be $< 33^{\circ}$ and is probably close to zero. If the minimum pitch angle $\sim 0^{\circ}$, then the angle between the spin axis and the detector axis is $\alpha + \gamma \sim 65^{\circ}$; see Fig. 3.5a. On the other hand, when the pitch angle coverage is a minimum (Fig. 3.5(b)), some spin modulation is still apparent in some records. This modulation implies that α and γ must differ by some moderate amount, perhaps 10 or 20°.

A well-modulated record (No. 52) was chosen, and several values of α and γ were used to generate plots similar to Fig. 3.4. The theoretical calculations showed that the spin phase and the amplitude of the range of pitch angles covered during a spin period were modulated by the coning motion. It was found that for $\alpha < \gamma$, the spin phase was modified in such a way as was obviously not occurring in the particle data. Therefore, it was evident that $\alpha > \gamma$. In that case, the apparent spin rate, averaged over a coning period, is equal to

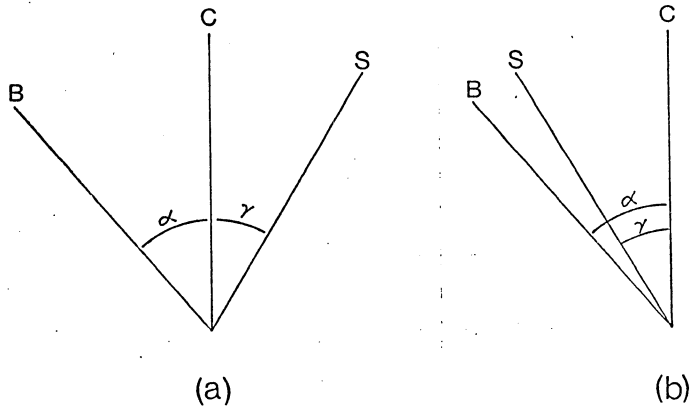

Fig. 3.5 Illustrating the two extreme cases of the relative orientations of the spin axis S and the magnetic field vector B. In case (a) the pitch angle coverage during a spin cycle will be a maximum; in case (b) it will be a minimum.

the sum of the true spin frequency in the body frame of reference, and the coning frequency.

Figure 3.4 shows the result finally derived, with $\alpha = 40^{o}$ and $\gamma = 30^{o}$.

The constants having been determined, the formulas (4) and (5) can be used to determine the pitch angle sampled by the detectors on the two sections of the payload as a function of time throughout the flight.

3.3 Effects of the Atmosphere on the Distribution of Precipitated Particles

The data to be analyzed were obtained at altitudes below 200 km. Hence, the effects of the atmosphere on the intensity of electrons in the energy range 1 - 10 kev must be considered.

The effect of interactions with the atmosphere is to modify both the energy spectrum and pitch angle distribution. Several authors have examined the loss processes, and some conclusions can be drawn about the validity of observations of these quantities. Rees (1963, 1964), Berger et al. (1970) and Kamiyama (1966) examined the ionization rate, which is proportional to the energy loss per unit path length, as a function of depth of penetration into the atmosphere for monoenergetic electrons incident on the top of the atmosphere. Their values for the altitude of peak ionization rate agree well. The results are remarkably independent of the initial pitch angle distribution.

The detailed results differ somewhat, but from the profiles of ionization as a function of altitude, it appears that a flux of 2.5 kev electrons should be significantly degarded at altitudes below

200 km. Ten-kev electrons are not affected to a measurable extent, while the effect on 5-kev electrons is marginally detectable only at the highest pitch angles.

Secondary electrons produced by the interactions of electrons with energy > 2.5 kev should not contribute significantly to the intensity at 2.5 kev. The spectrum of secondary electrons is orders of magnitude below the primary spectrum at all energies (Stolarski, 1968). Thus the intensity at 10 kev observed here could not be responsible for a measurable increase in the intensity at 2.5 kev. Higher-energy primaries may produce a higher proportion of 2.5 kev secondaries, but the primary intensity above 40 kev is typically observed to be a factor of at least 10^2 less than that at 10 kev under similar auroral conditions. In addition, at these energies, the proportion of the primary energy lost above 150 km, and thus available for the production of secondary electrons is $< 10^{-4}$ times the primary energy. Thus, even though the energy of the electrons may be 10^2 times the energy of the secondaries of 2.5 kev, the total energy actually available for the production of secondaries could produce only 10^{-4} times the observed intensity at 2.5 kev. The fact that in the data from rocket 18.17, significant changes in the intensity at 10 kev occur with no observable effect at 2.5 kev also strongly indicates that secondary electrons are insignificant in these data.

A third possible effect of atmospheric interactions to be considered is the modification of the pitch angle distribution. No adequate treatments of this problem exist. At first it might appear that the effect of atmospheric interactions should be to produce

a field-aligned distribution by removing the particles with higher pitch angles, because these travel a great path length in the atmosphere to reach a given altitude. However, electron-ion collisions produce large-angle scattering of the electron because of its much smaller mass. The loss in energy is typically small compared to the total electron energy. The result of these collisions is a tendency towards isotropy. The net effect is impossible to estimate on the basis of any simple analysis.

However, examination of the data suggests that the tendency is towards isotropy. As will be seen later, increases in pitch angle anisotropy are always greatest at 10 kev. While it is not certain that the same mechanism is responsible for the changes at all energies, the fact that, apart from a field-aligned "burst", the intensity at 2.5 kev tends to remain more isotropic supports the idea that the effect of atmospheric interactions is to produce an isotropic distribution.

3.4 Relationship Between Electron Data and Auroral Forms in the Trajectory

An overview of the data is shown in Fig. 3.6. As mentioned in Section 3.2, the detectors in the rear section scan in pitch angle from 33^{o} to 98^{o}. The loss cone half angle at the rocket altitude is approximately 90^{o}. Thus virtually all the electrons counted are precipitating. A useful first look at the data can be obtained by simply summing the counts in each detector over each digital record, producing averages over very nearly one second. The result is shown in Fig. 3.6, for the three detectors on the rear section and the

Fig. 3.6 One-second average electron data from the three fixed-energy channels on the rear section and the 10 kev channel on the forward section, together with parameters derived from this data. The spectral index indicates relative "hardness" of the spectrum on a scale 0 through 5. The anisotropy ratio J(35)/J(85) is the ratio of the intensity in the pitch angle interval 32^{o} - 40^{o} to that in the interval 80^{o} - 90^{o}, averaged over each record. The visible aurora record indicates the times that either discrete or diffuse aurora were visible at the location of the rocket. The precipitated energy is simply the sum of the energy flux measured by the 3 rear section detectors over each one second record.

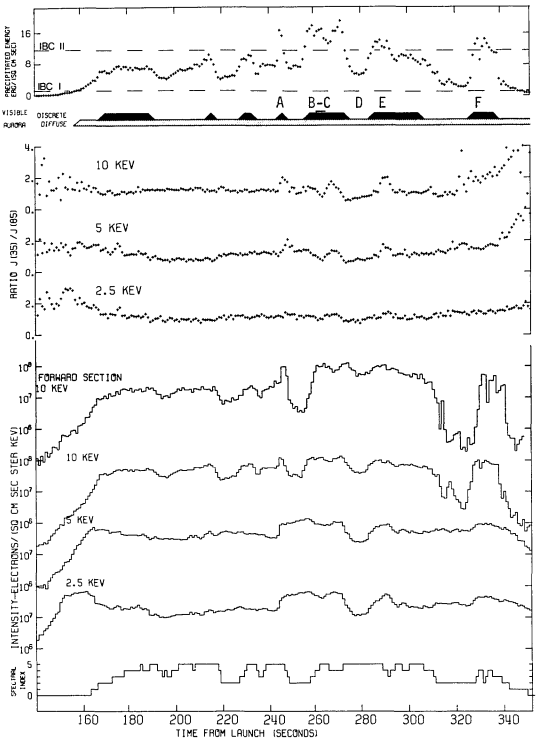

10 kev detector on the forward section. The count totals have been multiplied by the appropriate factor to produce directional intensities averaged over each record.

Comparison of the 10 kev data from the two sections reveals the following:

(i) The forward section data generally shows a greater variation from record to record. This is an effect of the coning motion which has a period of $\sim$ 2.5 sec.

(ii) There is a one-to-one correspondence between the features of each record greater than two or three sec duration.

(iii) The variations in the data from the forward section show a time delay relative to the corresponding variations in the rear section data. This delay is near zero at the beginning of the record, and increases to $\sim$ 2.5 sec towards the end. This delay implies that the variations are spatial in origin. It also indicates that the effect of separation was to give the forward section a negative velocity component relative to the velocity of the rear section. This would require a significant torque perpendicular to the main axis of the rocket, which could account for the severe coning effect apparent in the data. As will be derived later, the ground speed of the rocket was $\sim$ 0.51 km sec^{-1}. The observed average delay between the corresponding variations in the data from the two sections amounts to $\sim$ 2.5 sec in a total time of $\sim$ 300 sec. Thus the effective ground speed of the forward section relative to the rear section is $\sim$ 4 m sec^{-1}.

(iv) The magnitude of the maxima in the intensity measured by the forward section detector agree well with those recorded by

the rear section. However, below the maxima, there is a variation in the relative values which suggests that the sensitivity as a function of intensity is quite different for the two detectors. This variation was not expected on the basis of the laboratory calibrations of these detectors. Calibrations show that the counting efficience is a constant up to a count rate of at least 2×10^4 sec^{-1} and usually no serious degradation occurs below a count rate of 4×10^4 sec^{-1}, corresponding to an intenaity of $\sim 1.5 \times 10^8$ cm^{-2} $ster^{-1}$ kev^{-1}. In any event, the tendency is for the efficiency to be constant at lower count rates, whereas the data in Fig. 3.6 suggests that the efficiency continues to be a function of intensity down to the lowest intensities recorded.

The lack of an explanation for this discrepancy between the count rates of the two detectors further adds to the uncertainty of the absolute values of any spectral parameters derived from these data, already severely limited by having measurements at only three fixed energies. However, it is clear from the data shown in Fig. 3.6 that there are changes in the spectrum through the flight, for instance between T = 242 seconds from launch and T = 252. To give some idea of the changes in the spectrum through the flight, a spectral index was devised as follows.

Let a, b, c be the intensities averaged over one record for the energies 2.5, 5, 10 kev, respectively. Then a value for the spectral index was assigned to each region according to the scheme shown in Table 3.1. It can be seen that increasing values of the index corresponds to increasing "hardness" of the spectrum.

TABLE 3.1

DERIVATION OF THREE POINT SPECTRAL INDEX

INDEX	INTENSITY DISTRIBUTION
0	a > b > c
1	b > a > c + ½(b-c)
2	b > a b > c
3	b > c > a + ½(b-a)
4	b + ½(b-a) > c > b > a
5	c > b + ½(b-a) > b > a

The value of this spectral index derived for each record is plotted in Fig. 3.6. It can be seen that the index is > 0 for most of the flight. Values of the index > 0 indicate the existence of a peak in the spectrum, as is illustrated by the representative three-point spectra shown in Fig. 3.7. The examples were chosen at random except for that labelled T = 247 which is the most energetic records. The energy of the peak increases with the spectral index, being $\sim$ 5 kev for index = 3 and > 10 kev for index = 5. Also shown for reference in Fig. 3.7 is a Maxwellian energy distribution with kT = 10 kev. It is apparent that it is difficult to match the observed spectra to the form of a Maxwellian distribution.

The spin modulation evident in the relatively raw data, some of which are shown in Figs. 3.3 and 3.4, indicate that there is substantial structure in the pitch angle distribution. To obtain an idea of the variation of the pitch angle distribution, the ratio of the intensity between 30^{o} and 40^{o} (J(35)) to that between 80^{o} and 90^{o}

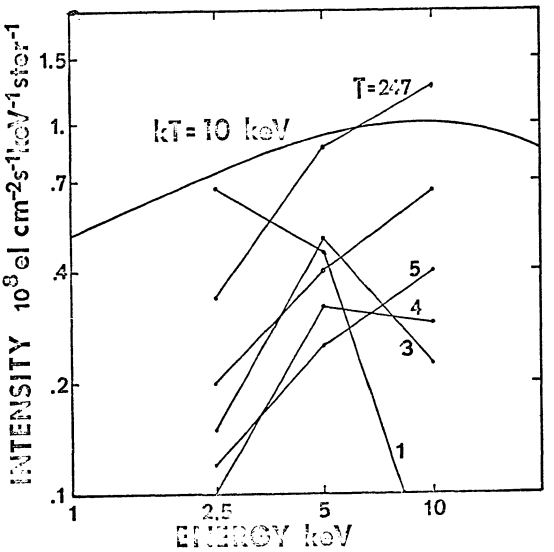

Fig. 3.7 Representative spectra from various points of the trajectory illustrating spectral indices, 2, 3, 4, 5 and showing the spectrum at the point of greatest energy flux at T = 247. For comparison a Maxwellian spectrum with kT = 10 kev is also plotted.

was averaged over each record for each energy. The results are plotted in Fig. 3.6.

Also plotted in Fig. 3.6 is the total precipitated energy measured in the bandpass of the detectors and summed over the one second interval of each record. The total precipitated power is certainly greater than the values plotted, but the data may be used to indicate the relative changes during the flight. As it is formed by simply summing the detector responses, the plotted value is weighted by the spectral information contained in the three channel data.

In order to obtain an approximate value for the total precipitated energy, the spectrum at T = 247 sec shown in Fig. 3.7 was integrated from E = 2.5 kev to E = 10 kev yielding a precipitated energy flux of $\sim$ 22 erg cm^{-2} sec^{-1}. This time, T + 297 sec, corresponds to the peak intensity measured in the southern limb of a westward propagating fold to be discussed later. The form of the spectrum (spectral index = 5) indicates the existence of a peak at energy $\lesssim$ 10 kev. Thus it is likely that a considerable contribution to the precipitated energy came from electrons with energy > 10 kev. The assumption that an equal contribution came from electrons with energy > 10 kev results in a precipitated energy flux of $\sim$ 44 erg cm^{-2} sec^{-1}. Examination of the scanning photometer record for this time shows a peak intensity in λ4278 in the arc of $\sim$ 20 kR. The ratio of intensity to precipitated particle energy is then $\sim$ 0.5 kR erg^{-1}, which is within a factor of 2 of more accruate measurements (Dalgarno et al., 1965).

In the cases where the spectral index is < 5, indicating that there is a peak at some energy < 10 kev, it is most likely that the

major contribution to the precipitated energy is carried by electrons with energy < 10 kev. Thus most of the precipitated energy is carried by electrons with energy in the range spanned by the three detectors.

Therefore, it is concluded that variations in precipitated energy flux between times when the spectral index = 5 and when it is < 5 are greater than implied by the variations in the data shown in Fig. 3.6.

On the assumption that the intensity of auroral emissions λ4278 and λ5577 is approximately proportional to the precipitated energy, it should be possible to identify the features of the precipitated energy record with features of the visible aurora as recorded by the all-sky cameras and scanning photometers.

The six most distinct features of the precipitated energy record are identified in Fig. 3.6 by the letters A through F: five maxima and one minimum. These features have been matched to features of the visible aurora along the rocket trajectory, as recorded by all-sky cameras and scanning photometers. For this purpose, it was assumed that the azimuth of the trajectory was $\sim 5^{o}$, as indicated by the radar data, and that the horizontal speed of the rocket was constant.

Figures 3.8 and 3.9 present a summary of these data obtained from Fort Yukon at approximately 0819:23, corresponding to the time occurrence of peak A. The all-sky photograph in Fig. 3.9 is an 8-second exposure. Frames with shorter exposures around the time of that shown reveal more details of structure in the brighter forms, but do not show the fainter forms. The apparent lower borders of the identifiable arcs in the photograph were mapped onto a horizontal

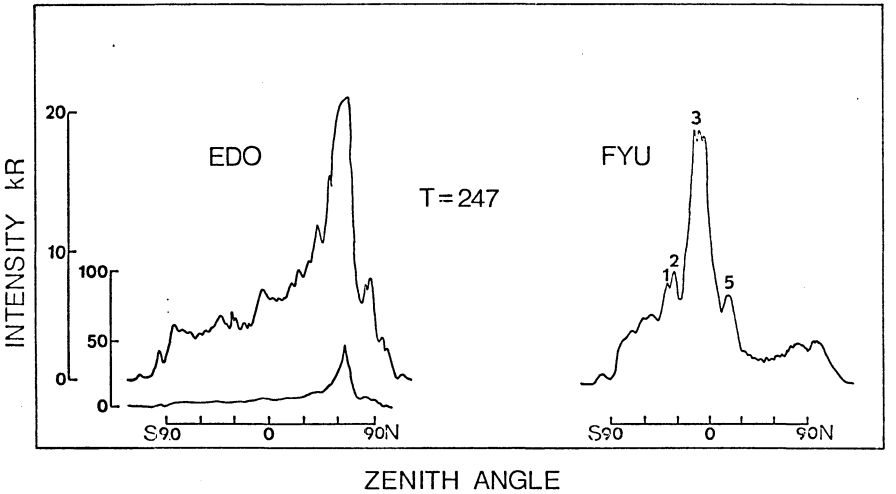

Fig. 3.8 Scanning photometer traces at T = 247 from Ester Dome Observatory (EDO) and Fort Yukon (FYU) showing the measured intensity as a function of zenith angle in λ4278.

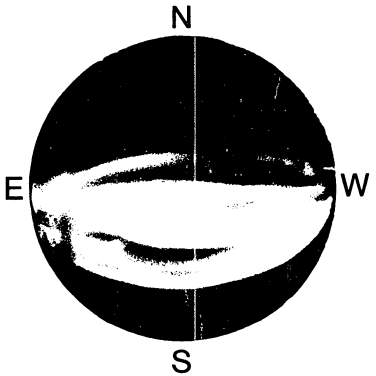

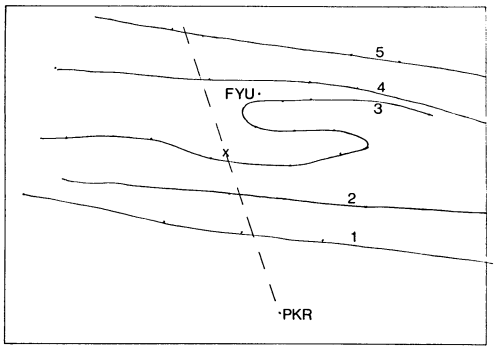

Fig. 3.9 Relationship between the visible auroral forms as recorded by the Fort Yukon all-sky camera and the rocket trajectory at T = 247. The auroral arcs were mapped onto a horizontal plane assuming a lower border height of 110 km. The position of the rocket, mapped down the field line to that altitude is shown by a cross.

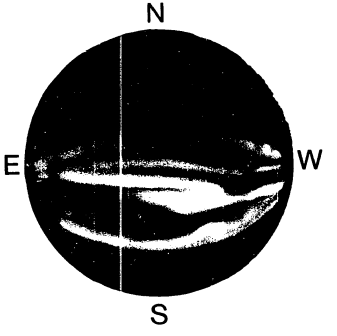

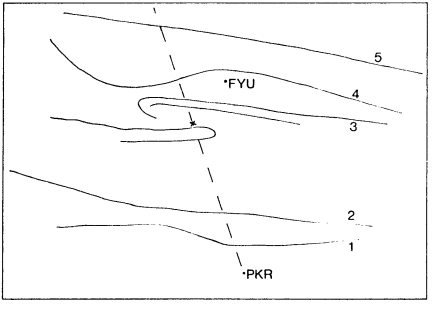

Fig. 3.10 As for Fig. 3.9 at T = 267.

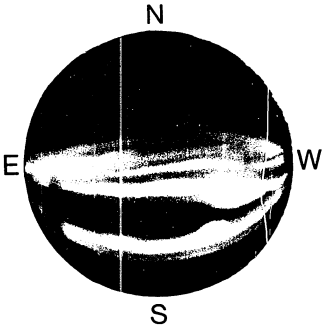

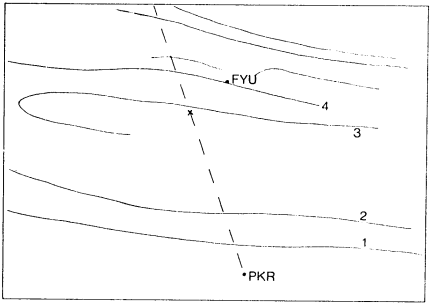

Fig. 3.11 As for Fig. 3.9 at T = 287.

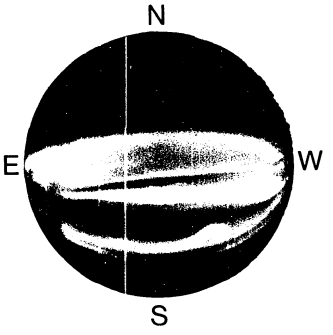

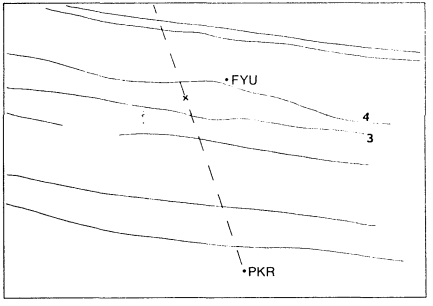

Fig. 3.12 As for Fig. 3.9 at T = 307.

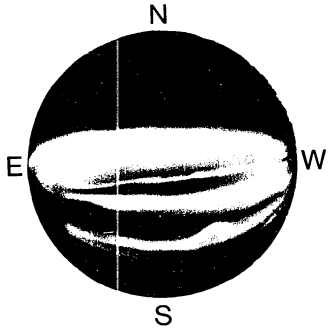

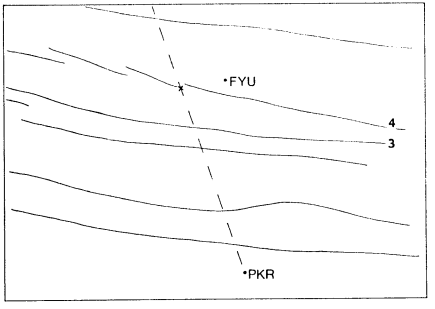

Fig. 3.13 As for Fig. 3.9 at T = 327.

plane, assuming a lower border altitude of 110 km. This value was obtained from the scanning photometer data by triangulation of the more southerly arcs which were identifiable from both Fort Yukon and Ester Dome. The arcs nearer to Fort Yukon were probably lower, but for the smaller zenith angles involved the error is not significant. The scanning photometer traces in λ4278 from Ester Dome and Fort Yukon are shown in Fig. 3.8 with the peaks numbered to correspond to the arcs numbered in Fig. 3.10. The arcs numbered 1 and 2 appeared after the rocket had passed their location as can be seen by comparison with Fig. 2.6. Consequently, there are no features of the particle record which can be related to these arcs.

Figures 3.10 through 3.13 show the positions of the various arcs as recorded at Fort Yukon at 20 second intervals. The rocket trajectory is plotted on each diagram.

It was found that the best fit was obtained by assuming an equivalent horizontal speed of 0.51 km sec^{-1}. Using this speed, the location of the rocket relative to the aurora at an altitude of 110 km is marked by an X in Figs. 3.9 through 3.13.

The first well-defined arc penetrated by the rocket is that numbered 3 in Fig. 3.9. The indicated position of the rocket appears a little to the north of the arc, but the arc was moving rapidly throughout this period. The motion could easily account for the discrepancy. It appears that at T = 260 (feature B) the rocket penetrated the southern limb of the fold. Examination of the all-sky photograph in Fig. 3.10 shows that this part of the arc is not well defined. The surrounding shorter exposures do not resolve the arc, but show a complex multiple

structure in the immediate vicinity. On this basis, it appears that peak C was also caused by the irregular movement of this same arc.

By T + 280, the rocket had moved clear of the southern limb of the fold into a region of relatively low energy deposition, and at T + 287 it encountered the northern limb (Fig. 3.11). Meanwhile, the region of relatively homogeneous diffuse arcs to the north of the westward propagating fold had become more structured. By T + 307, the rocket had moved clear of arc 3, and arc 4 had become quite well defined and more intense (Fig. 3.12). At T + 327 (Fig. 3.13) the rocket encountered arc 4, which had become active, and exhibited rapidly propagating fold structure.

From approximately T = 300 on, the TV systems at Ester Dome and Fort Yukon showed $\sim$ 10 Hz flickering (Beach et al., 1968) in arcs 3 and 4. Before T = 300, the cameras were not pointed in a suitable direction, so the possibility that flickering was occurring through the whole period of interest is not precluded. Indeed, the morphology of the aurora suggests that it quite likely was flickering (T. J. Hallinan, private communication).

The trajectory for the rocket having been established, partly by comparison of the ground-based auroral data and data from the particle detectors, it is possible to examine the relationship between the less obvious variations in the precipitated energy flux and visible auroral features. Of particular interest is establishment of an approximate threshold for the precipitated energy flux required to produce a visible aurora. For this purpose the data from T = 150 through T = 246 were examined in detail. As seen in Fig. 2.6, at the time

of launch there was no aurora visible in the region later occupied by arcs 1 and 2 in Fig. 3.10. However, by T = 100 a broad diffuse arc appeared and moved slowly southward. This arc corresponds to the broad peak in the precipitated energy flux between T = 170 and T = 193.

Detailed examination of the structure of the aurora in the vicinity of the rocket through this period is made difficult by the reflection of artificial lighting in the south and southwest quadrants of the Fort Yukon all-sky photographs. Meridian scanning photometer data cannot be used, as the scanning plane is different from the rocket trajectory, and the detailed structure of the aurora shows significant longitudinal variations.

At T = 217, a faint auroral feature appears very close to the predicted position of the rocket, It probably corresponds to the peak energy flux observed near that time. Near T = 225, there is an obvious minimum in visible light at the rocket, but the photographic image shows some density. Some of this density may be due to emissions at greater altitudes further from the rocket. It is not possible to reproduce these photographs, as small variations in intensity are obscured in reproductions other than those made directly from the original negatives. Near T = 325 there is also a distinct minimum in the exposure of the all-sky photograph at the expected location of the rocket but again some density is evident. The examination of these minima indicates that the threshold energy flux for the production of a detectable aurora as recorded by the all-sky camera is $\sim$ 1.2 erg cm^{-2} sec^{-1}. This value is a factor of $\sim$ 2 higher than estimates

of the energy influx required to produce an aurora of International Brightness Cocefficient I (Dalgarno, et al. 1965). For reference, the observed level of detectability of visible aurora was labelled IBC I on Fig. 3.6. A second threshold for the production of an IBC II aurora was identified on the assumption that the energy influx required is 10 erg cm^{-2} sec^{-1}. However, the identification with the brightness coefficients should only be regarded as approximate due to the incomplete nature of the electron spectrum used in the computation of the energy flux.

Figure 3.14 presents a summary of the features of the precipitation pattern as observed from the rocket and from the ground. Those features whose properties were determined primarily from particle data are shown by the patching extended to above the 200 km level. The features of the diffuse aurora are shown with the field-aligned extent of the patching approximately proportional to the intensity of the aurora at the time that the rocket was situated on the corresponding field line. Thus the diagram does not represent the situation at any one instant in time.

3.5 Electron Pitch Angle and Spectral Distributions

Some idea of the variation in pitch angle distribution through the flight can be obtained from the curve J(35)/J(85) in Fig. 3.6 which shows the ratio of the intensity at $\alpha = 35^{o}$ to that at $\alpha = 85^{o}$ averaged over a record length ($\sim$ 1 sec) for each of the three energy channels.

It will be noticed that over most of the flight, the higher the precipitated energy the more anisotropic the intensity. This

relationship is not true near T = 150 sec, where the 2.5 kev channel shows a strong field-aligned distribution, but the total precipitated energy is quite low. Figure 3.15 shows pitch angle distributions for the three energies at points between T = 150 and T = 240. Through this period, the rocket is in a region of low auroral luminosity.

As indicated by the spectral index at the bottom of Fig. 3.6, the spectrum appears to be very soft at the beginning of the data records shown in Fig. 3.6, becoming increasingly hard with time. However, there is also considerable variation over short periods as can be seen, for example, by comparing the examples in Fig. 3.15.

At T = 156, the spectrum is very soft, with the 2.5 kev electrons showing a strong peak at low pitch angles. The 5 kev electrons are isotropic, while the 10 kev electrons show a slight peak towards the lowest pitch angles. The combined effect of these different pitch angle distributions is to produce a hardening of the spectrum with increasing pitch angle. The altitude of the rocket at this time was approximately 175 km on the upleg.

From T = 156 to T = 233 there is an overall tendency towards isotropy. At T = 167 the 10 kev electrons are nearly isotropic for $\alpha < 80^{o}$. The 2.5 kev and 5 kev electrons are somewhat field-aligned, and the spectrum shows a distinct peak at 5 kev. The spectral index in Fig. 3.6 shows steady increase through the period T = 160 to T = 190. By T = 199 the 2.5 kev electrons have become essentially isotropic and show only small variations in pitch angle distribution through the remainder of the flight, as indicated in Fig. 3.6. Changes in the energy spectra are due mainly to changes in the 5 and 10 kev

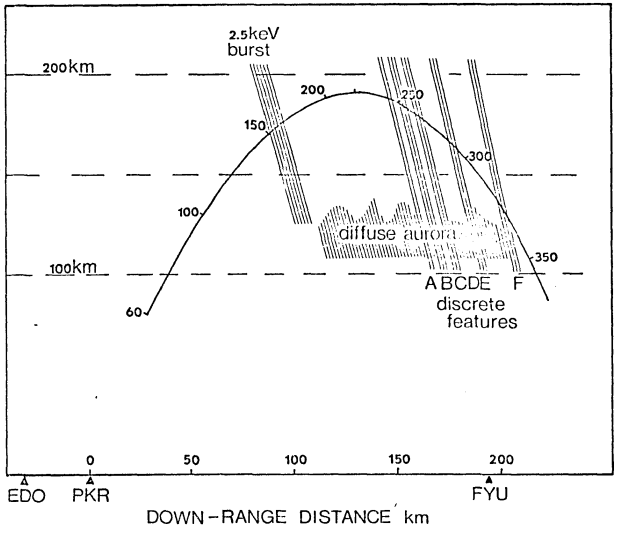

Fig. 3.14 Approximate profile of the rocket trajectory as finally determined. The locations of the pricipal features of the aurora or the particle data are shown at the time of penetration by the rocket. Thus, the diagram does not show the locations of the features at any one instant.

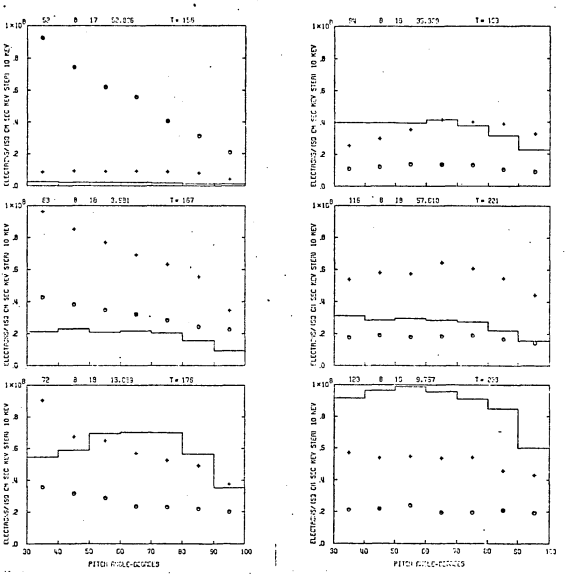

Fig. 3.15 Pitch angle distributions averaged over 10 degree intervals of precipitated electrons in the region, south of the main arc system. The solid line represents the 10 kev data, the circles and crosses, the 2.5 kev and 5 kev data respectively.

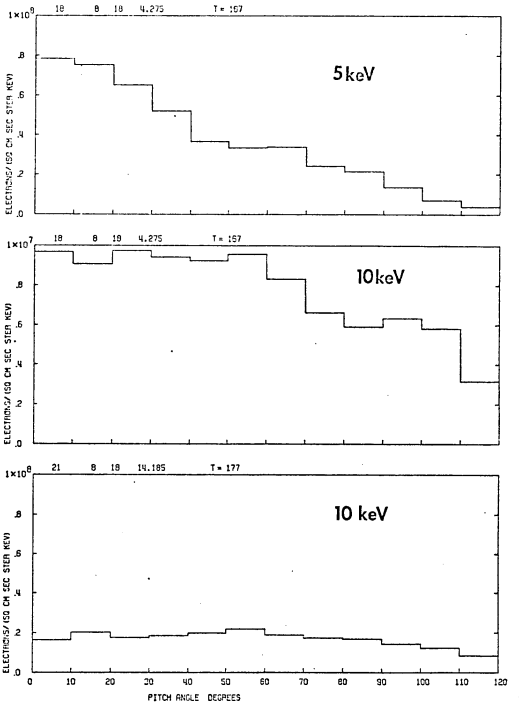

Fig. 3.16 Forward section data corresponding to T = 167 and T = 176 in Fig. 3.15.

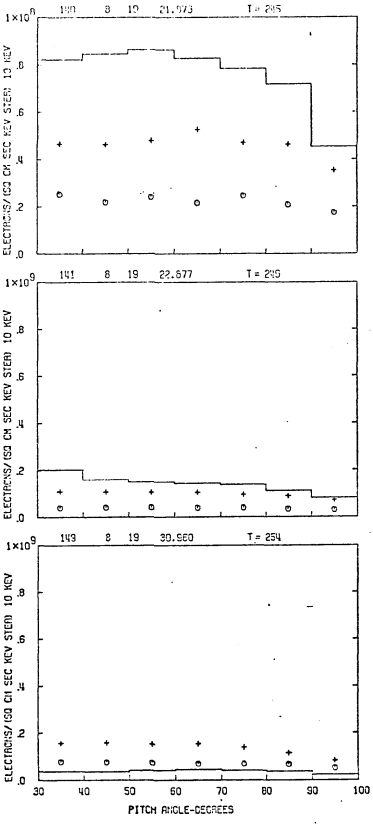

Fig. 3.17 Pitch angle distributions near the southernmost bright arc. Note the scale change between T = 245 and T = 246.

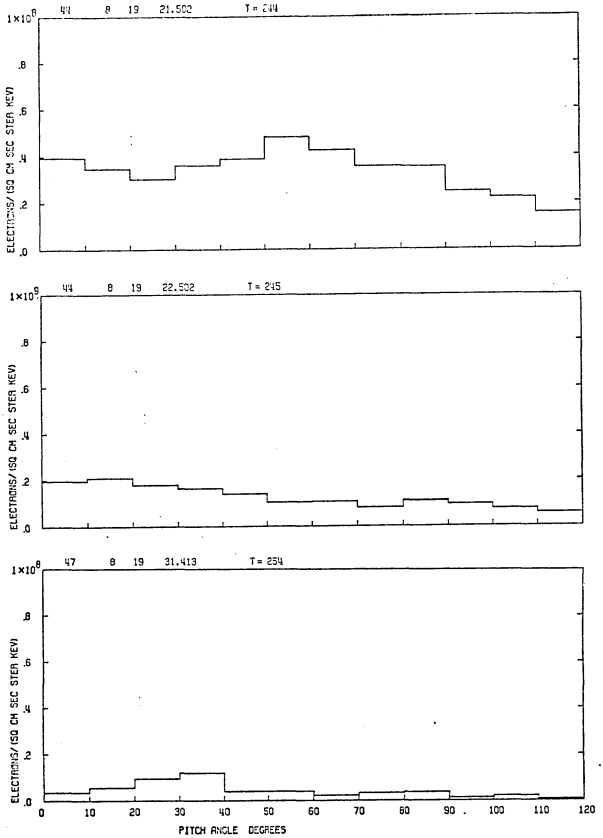

Fig. 3.18 Pitch angle distributions of 10 kev electron intensity measured as the forward section penetrated the southernmost bright arc.

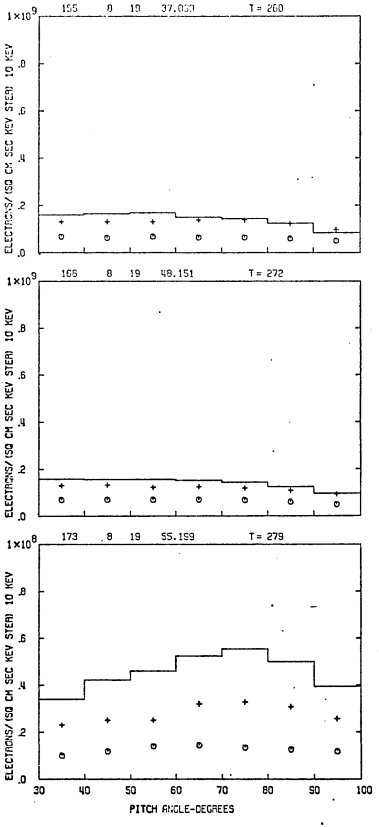

Fig. 3.19 Pitch angle distributions at peaks B and C and at the minimum in precipitated energy, D.

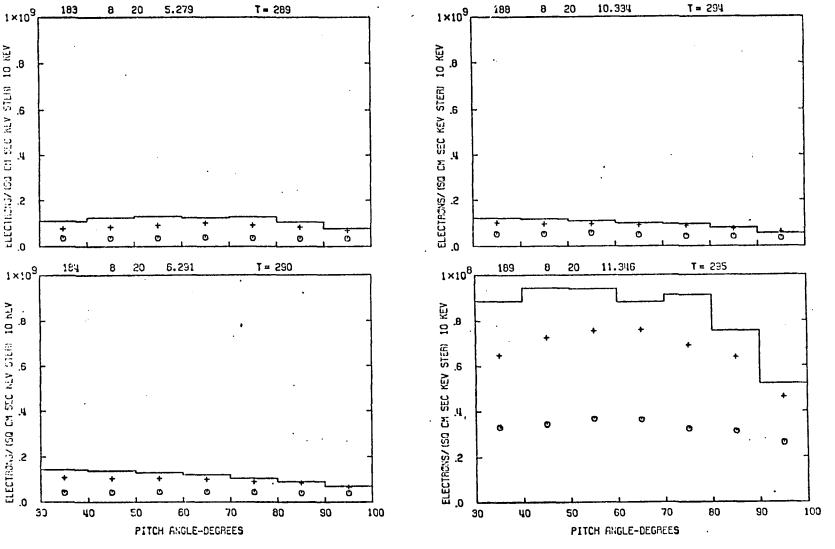

Fig. 3.20 Pitch angle distributions around peak E.

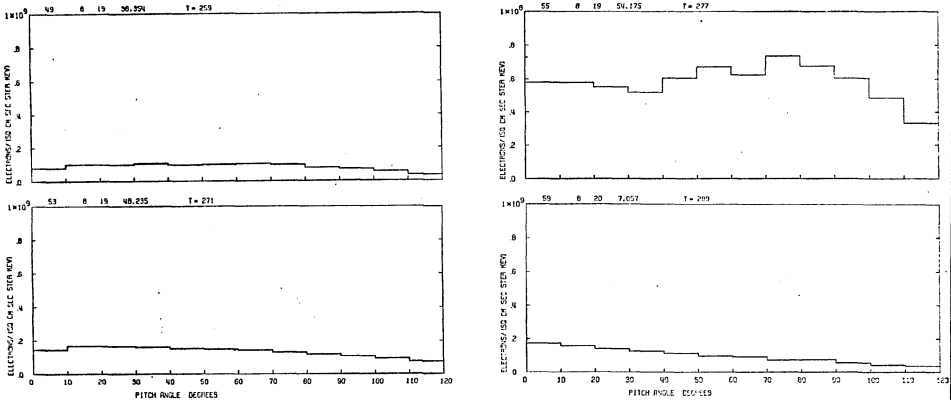

Fig. 3.21 Forward section pitch angle distributions at peaks B, C, E and *minimum* D.

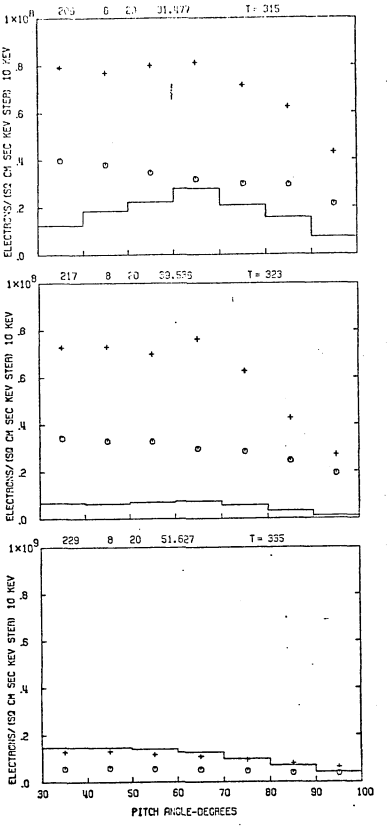

Fig. 3.22 Pitch angle distributions near peak F.

intensity.

Figure 3.16 shows the 5 and 10 kev pitch angle distributions obtained on the forward section at T = 167 and the 10 kev at T = 177. The 5 kev detector ceased functioning at T = 180. The 5 kev intensity is seen to be strongly field-aligned at T = 167, and the tendency of the 10 kev intensity towards isotropy is seen to extend to zero pitch angle.

It can be seen that the pitch angle distribution of 10 kev electrons as measured on the forward section is similar in form, if not in magnitude, to that measured on the rear section. The fact that it is almost impossible to find identical scans over the pitch angle range common to the data from the two sections is thought to be due to the electron precipitation being structured both in space and time over the whole region of interest. This effect is apart from the overall difference in the detector response discussed earlier.

At T = 246, the rocket enters the first bright arc, corresponding to peak A on Fig. 3.6. Figures 3.17 and 3.18 show the pitch angle distributions in consecutive records at the southern edge of the arc, and shortly after the rocket has cleared the northern edge. The change from nearly isotropic to a field-aligned distribution is apparent. Again note the scale change between T = 245 and T = 246. At T = 246, the spectrum softens towards larger pitch angles. At T = 254 the spectrum has become soft (spectral index = 3); the softness can be seen from Fig. 3.6 to be due entirely to a decrease in the intensity of 10 kev electrons.

Figure 3.19 shows pitch angle distributions at T = 260, cor-

responding to peak B; T = 272, peak C; and T = 279 at the minimum in the precipitated energy, D. The distributions in the peaks are not as strongly field-aligned as in the case of A. However, the aurora in this region was not as well-defined as in peak A. The pitch angle distribution at D (T = 277) shows a definite peak near 80^{o} in both 10 and 5 kev channels, and even a broad peak near 65^{o} in the 2.5 kev channel. The 10 kev data from the forward section show distributions similar to those near peak A; in the arcs the intensity increases towards $\alpha = 0$, and at T = 277, away from the arc, the intensity decreases or remains fairly constant as $\alpha \rightarrow 0$.

As the rocket nears peak E, corresponding to arc 3 in Fig. 3.12, the 10 kev pitch angle distribution again changes from one showing a broad peak around 60^{o}, to one more field-aligned. The transition is abrupt, as can be seen by comparing the data in Fig. 3.20 for T = 289 which shows a broad peak at $\sim 60^{o}$ and T = 290 which shows a maximum at 30^{o}. On the northern side of the arc, the transition is similarly abrupt as shown by the consecutive records at T = 294 and T = 295. However in neither case is the change as pronounced as in the data near T = 247 at the southern edge of the fold structure.

Figure 3.21 shows the extended 10 kev pitch angle distributions from the forward section corresponding to peak B (T = 259), peak C (T = 271), minimum D(T = 277) and peak E (T = 289). It is seen that the characteristics inferred from the rear section data are confirmed.

At T = 295 the rocket was at an altitude of 160 km on the downleg. Beyond this time, the altitude becomes low enough that atmospheric

interactions cannot be ignored in considering the lower-energy data.

After T = 295, the distributions remain fairly isotropic, with the intensity of the 10 kev electrons decreasing steadily so that the spectrum becomes softer. The data for T = 315, in Fig. 3.22, are typical of this region. By T = 323, the spectrum appears to be strongly peaked near 5 kev for pitch angles less than $\sim 60^{\circ}$, and there is some tendency for the intensities at both 5 and 10 kev to be field-aligned. Finally, at peak F, the intensities at all energies are field-aligned (T = 335 in Fig. 3.22), and from this point on, a general decrease in count rate in all channels is probably the result of atmospheric attenuation.

The detailed analysis of the pitch angle and energy distributions shows that the parameters J(35)/J(85) and the spectral index plotted with the other data in Fig. 3.6 can be used to completely characterize the electron distributions as measured over the entire data record. The pitch angle relationships observed are summarized as follows.

(i) Increases in the ratio J(35)/J(85) over the value 1.5 imply that the distribution is field-aligned in that the intensity decreases by that factor over the pitch angle range 35° to 90° in the case of 10 kev electrons. With some notable exceptions (e.g., near T = 325) the decrease is monotonic over that range. The spectrum is generally harder at the lowest pitch angles.

(ii) Values of the ratio J(35)/J(85) near 1.0 indicate an isotropic distribution, perhaps showing a broad peak near 60°.

Occasionally through the flight, an unusual pitch angle distribution is seen. The best example is shown in Fig. 3.23. It shows a sharply

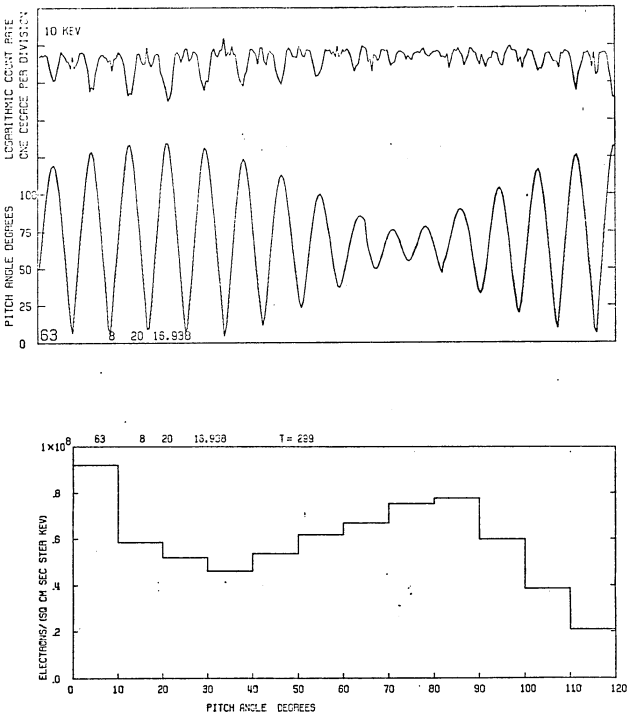

Fig. 3.23 Showing the characteristic triple peaked pitch angle scan (top) produced by the distribution shown below.

field-aligned peak superimposed on a pitch angle distribution with a minimum near 30^{o}. This distribution produces a triple peak in the spin modulation which is easily identifiable. Less spectacular examples occur near T = 167, 220, 256 and 274. Note that these times correspond to instances of relatively low precipitated energy. Such instances are otherwise characterized by pitch angle distributions in the higher energy channels which are either isotropic or which show a decrease towards 30^{o}. This result is remarkably similar to one reported by Whalen and McDiarmid (1972).

CHAPTER 4

PARTICLE-AURORA MORPHOLOGY

4.1 Summary of Observations

At T $\sim$ 150 the rocket, moving northward, passed from a region of near-zero electron precipitation into a region characterized by a "burst" of 2.5 kev electrons lasting until T $\sim$ 160. The pitch angle distribution of these electrons was peaked at $\sim 35^{\circ}$, the lowest pitch angle measured. The intensity of 5 and 10 kev electrons remained low during this period, so that the spectrum was very soft, as indicated by the three point spectral index, and the total energy influx was below the threshold for the production of a visible aurora.

Between T = 170 and T = 246, the rocket passed through at least three identifiable, though relatively diffuse, weak auroral forms. The spectral index indicates a general increase in hardness throughout this period. From T = 172 on, the index is ≥ 3, indicating the existence of a peak in the spectrum at some energy $\gtrsim 5$ kev. The index is also seen to increase at times of higher precipitated energy flux, identified with visible auroral forms. The intensity at all energies was fairly isotropic through this period.

Between T = 247 and T = 300, the rocket passed through a westward propagating fold in a bright, auroral arc thus crossing the arc three times. The spectral index was 5 at the peak of each crossing, implying a spectral peak at $\gtrsim 10$ kev. The intensities at the higher energies were peaked at low pitch angles. The background spectrum changed systematically as the rocket crossed and re-crossed the arc, in such a way as to indicate that the arc separated regions of different

characteristic spectrums, and that the separation followed the form of the fold.

Northward of the fold, the rocket passed through a region of diffuse aurora, and at T = 330 penetrated another bright arc, characterized by an electron spectrum peaked near 5 kev. Thereafter the particle record shows a characteristic decrease in intensity as the vehicle altitude decreased.

Examination of the measured characteristics of the electrons through the data record yields several observational results. These results form the basis for the ensuing discussion, and are listed below in summary form.

(i) The delayed correspondence between the 10 kev data from the two sections of the payload shows that the main features observable in the one-second average data were spatial in origin.

(ii) A threshold value of the precipitated energy flux was apparent for the production of a visible aurora. This value corresponds approximately to that required to produce an IBC I aurora.

(iii) There was a detailed correspondence between the variations in the particle data and features of the visible aurora.

(iv) A field-aligned "burst" of 2.5 kev electrons was recorded at the southern edge of the region of visible aurora.

(v) The spectrum in the background aurora and the weaker forms showed a peak $\sim$ 5 kev.

(vi) The spectrum in the brightest arc indicated a peak > 10 kev.

(vii) With the exception of the 2.5 kev "burst", the pitch

angle distribution was fairly isotropic in the background aurora and the weaker arcs. A broad peak $\sim 60^{o}$ was sometimes evident.

(viii) In the brightest arcs, the pitch angle distribution was field-aligned at 5 and 10 kev, with the strongest anisotropy at 10 kev. The distribution showed a smooth monotonic decrease with increasing pitch angle.

(ix) The previous two results show the existence of an intensity threshold for the occurrence of a field-aligned anisotropy. This threshold corresponds approximately to the energy influx required to produce an IBC II aurora.

(x) The folded arc formed a boundary between regions characterized by a relatively hard spectrum immediately to the south of the arc and a softer one to the north. The boundary appeared to follow the form of the fold.

(xi) A pitch angle distribution showing a strongly field-aligned peak superimposed on a non-isotropic distribution was sometimes observed, usually in association with the brightest arcs.

4.2 Comparison of observations with Previous Rocket and Satellite Data

The few seconds of relatively intense, field-aligned precipitation at 2.5 kev may correspond to the "bursts" of 2.3 kev field-aligned electrons measured on OGO-4 and described by Berko (1973). His analysis is mainly statistical and shows that on the average the bursts occur at the poleward edge of the region of maximum occurrence of auroras (Stringer and Belon, 1967) in the midnight sector. However, individual passes at fairly disturbed times as measured by the AE index show

simultaneous events at latitudes spanning the auroral zone. So the identification is reasonable.

Principally because the region covered by the rocket trajectory is one of fairly intense electron precipitation, it seems likely that it corresponds to an "inverted V" event observed by Frank et al., and Ackerson (1971), on the satellite INJUN 5 in polar orbit. These events typically extend over perhaps 150 km, a similar length to the data record discussed here. In these events, the maximum intensity occurs at low energies, rises to a few kev, and decreases again over a period of typically $\sim$ 40 sec as the satellite moves meridionally. In one example, the precipitated energy reaches a peak of $\sim$ 70 erg cm^{-2} sec^{-1}. The precipitated proton energy was a factor $\sim$ 100 lower through the pass.

These inverted V events are frequently observed, in fact, are a characteristic of regions of intense precipitation. The precipitated energy is certainly enough to produce a bright aurora. Ackerson and Frank (1972) identify an intense band of precipitation with an auroral arc recorded with an all-sky camera at Fort Churchill. The color spectrogram published by them does not show an obvious spectral peak. However, individual spectral scans do show a slight peak near 1 kev. The energy of the peaks in the spectra observed by Ackerson and Frank are typically $\sim$ 1 kev, and the spectra can be well approximated by a Maxwellian distribution with $E_o \sim 1$ kev superimposed on a decaying power law spectrum. This result agrees with the results of rocket-borne measurements by Westerlund (1969), Chase (1969), Rearwin (1971) and others obtained in diffuse aurora. The same type of spectrum

has been observed in regions of diffuse aurora associated with active, discrete arcs by Westerlund (1969), Bryant et al., (1973). The similarity between this type of spectrum, and typical spectra of plasma sheet electrons has been noted by several authors (Chase, 1969; Rearwin, 1971; Hones et al., 1971b; Frank and Ackerson, 1971; Johnstone et al., 1973). It is generally thought that these electrons have been energized by adiabatic compression produced by their convective motion.

At lower latitudes the electron spectra become less intense but harder, characteristic of the outer radiation belt. At the poleward edge, there is often a "slot" of very low intensity. A narrow (0.2^{o} of latitude), intense, low energy "precursor" occurs immedately poleward of this "slot".

The spectral information contained in the data from rocket 18.17 is not adequate for a detailed discussion. However, the results do indicate that it is difficult to match the data to a Maxwellian distribution even in the diffuse regions between the discrete arcs. Rather, the spectrum shows a peak at $\sim$ 5 kev throughout these regions.

These results are remarkably similar to those of Pazich (1973) who describes particle measurements made on one of the most successful auroral rocket flights. The rocket carried a vector magnetometer (Cloutier, et al., 1970) and several particle detectors. It was launched so as to penetrate a bright auroral arc which remained near the magnetic zenith at Fort Yukon throughout the flight. Magnetic records indicate that a medium-magnitude substorm was occurring in the Canadian sector during the flight with negative bays of

$\sim$ 200γ in H recorded at Fort Smith (dp lat 68.5°) and Fort Chipewyan (67.0°), and positive bays at lower latitude stations. The aurora over Fort Yukon brightened some time before the flight, and was very bright ($\sim$ 60 kR in λ5577) during the flight. Several westward propagating folds are evident in the all-sky camera record. It appears that the rocket actually crossed one of these folds. The visible aurora and geomagnetic effects are quite similar to those prevailing during the flight of rocket 18.17, although in Pazich's case, the situation seems to be a more clearly defined "expansive phase" of a substorm. The electron spectra showed a peak of a few kev during the time that the rocket was actually in auroral forms. In a relatively bright band to the south of the brightest band the peak was in the range 2 - 4 kev and the pitch angle distribution was strongly peaked at low pitch angles - that is, "field-aligned". A less intense region between the visible forms showed a spectral peak at $\sim$ 8 kev and an isotropic pitch angle distribution. In the brightest band, the pitch angle distribution is again field-aligned and the spectral peak is $\sim$ 10 kev. Data from this region are shown in Fig. 4.1. Northward of the band, the intensity and spectral peak fall away rapidly, and the intensity becomes isotropic with a monotonically decreasing spectrum.

The presence of the peaked spectrum as described by Pazich (1973) and observed on 18.17 in the region of diffuse aurora is difficult to relate to previous observations. Frank and Ackerson (1971) state that their published results are typical, and thus one expects that they would have noticed the occurrence of these

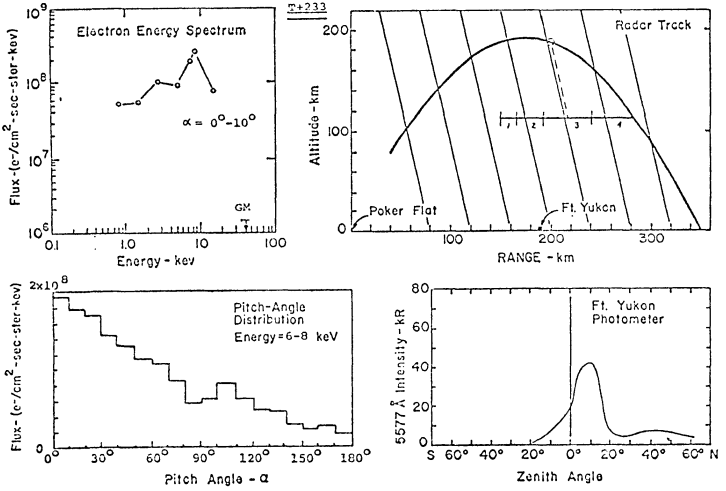

Fig. 4.1 Electron energy spectrum and pitch angle distribution obtained in a bright, folded arc under very similar auroral conditions to those prevailing on flight 18.17 (Pazich, 1973).

non-Maxwellian peaks if they were at all common. In the data published by Frank and Ackerson (1971), the lower intensity regions of the inverted V events invariably show a monotonically decreasing spectrum. This problem is not resolved at this stage.

It is possible that the occurrence of these peaked spectra is related to the phase of development of substorm activity. Both the observations of Pazich (1973) and those presented here were made in the latter stages of substorm activity centered to the east of the observations. The features of the visible aurora in the trajectory were remarkably similar in each case.

Two features of Pazich's (1973) results and those presented here do correspond to features of the inverted V events. In both cases, the bright, folded auroral arc marked a boundary between a relatively hard background electron spectrum to the south and a softer one to the north. This corresponds to the effect of passing through the northern boundary of an inverted V event. In addition, a little poleward of this boundary, another, isolated region of lower energy and lower intensity precipitation occurs both in the results of Pazich (1973) and those given here (Peak F). This region could well correspond to the poleward "precursor" described by Frank and Ackerson (1971). The northward edge of this "precursor" observed on the rocket flights marked a sharp cut-off in precipitated energy as indicated by the absence of auroral emissions, and again this is a characteristic of the results of Frank and Ackerson.

In the case of payload 18.17, another aspect of the boundary observed between the two characteristic background electron spectra

is that it appeared to follow the folded structure of the arc. From the results of Cloutier et al. (1970) and Park and Cloutier (1971) it is expected that in coincidence with a folded arc of such intensity and activity should be an intense ($\sim 10^{-5}$ A m^{-2}) field-aligned current. This was true in the case discussed by Pazich (1973). This correspondence suggests that such a field-aligned current is intimately related to the boundary between the different particle characteristics.

In the brightest arc, the spectrum peaks at some energy $\gtrsim$ 10 kev. Triangulation measurements carried out on these arcs using the meridian scanning photometer data from Fort Yukon and Ester Dome show that the altitude of the peak volume emission rates was 100 $\pm$ 2 km. This altitude implies a characteristic energy of the precipitating electrons of $\sim$ 12 kev (Berger et al., 1970). Detailed examination of the data shows that the spectrum is hardest in the brightest arcs, and that it is hardest at small pitch angles.

Observations of peaked spectra often referred to as monoenergetic, or as having a monoenergetic component, have been reported several times (McIlwain, 1960; Evans, 1968; Bryant et al., 1973). in those cases where the measurements were extended to low energies, it was found that the monoenergetic peak was superimposed on an otherwise monotonically decreasing spectrum, so that at some lower energy, usually < 1 kev, the intensity actually exceeded that at the peak (Westerlund, 1969). These peaked spectra occur in bright arcs associated with all phases of auroral activity and appear to be associated with the intensity of the arcs rather than any morphological aspect of substorm development.

CHAPTER 5

ACCELERATION AND PRECIPITATION MECHANISMS

5.1 Large-Scale Mechanisms

The characteristics of precipitating particles observed in this study and elsewhere can be divided into three classes. (1) Spectra similar to those found in the plasma sheet and inverted V events, i.e., monotonically decreasing with approximately an exponential form, sometimes with a Maxwellian-like peak superimposed. The pitch angle distributions are isotropic, or slightly peaked at pitch angles between 60^{o} to 90^{o}. (2) Spectra with sharp peaks at energies of a few kev and pitch angle distributions similar to the first class. (3) The most intense, with spectra peaked at energies of several kev and pitch angle distributions peaked at angles $< 30^{o}$.

Observations in class (3) are always made in active bright auroral arcs as was the case on payload 18.17. Observations in classes (1) and (2) are generally made in regions showing relatively less visible auroral activity. In the case of payload 18.17, the background aurora and the more diffuse arcs were characterized by distribution of class (2).

It is often assumed that the pitch angle distributions of classes (1) and (2) are derived from magnetosheath or plasma sheet particles which have been adiabatically compressed while being convected inwards towards the auroral field lines where they are observed. As the convection proceeds, the particle energy density increases. Also, the pitch angle distribution shows a decrease as $\alpha \rightarrow 0$ due to precipitation of particles in the loss cone. In the theory of Kennel and

Petschek (1966), this pitch angle anisotropy itself supplies the free energy for the generation of whistler mode waves, which scatter resonant particles into the loss cone. Particles are thus supplied to the system by convection and are precipitated by diffusion into the loss cone. In the case of "weak diffusion", particles diffuse into the loss cone in a time much less than the quarter bounce period of the particles; thus the loss cone remains empty. If the particle intensity increases, there is a transition to "strong diffusion" in which case particles diffuse into the loss cone in a time much less than the quarter bounce period, so the loss cone tends to fill, i.e., the pitch angle distribution tends to isotropy. Of course, it cannot become isotropic, or the energy source for the instability will disappear. The strong diffusion limit imposes an upper limit on the intensity of particles trapped on a given field line. To a first approximation, there is no diffusion in velocity space, i.e., the energy of the particles is unaffected. Thus it can be assumed that the energy spectra of the precipitated particles are identical to those of the source particles in the equatorial plane.

A signature of this mechanism is a more-or-less hollow loss cone, that is, a pitch angle distribution $f(\alpha)$ which shows a positive slope for $0^{o} < \alpha \lesssim 90^{o}$. This is, in fact, usually observed in regions of relatively low precipitated intensity.

The field-aligned pitch angle distribution of class (2) must be produced by some other mechanism, perhaps acting simultaneously with the process described above. Mechanisms capable of producing a field-aligned distribution which have been discussed in the literature

include the Fermi-betatron process and parallel electric fields. Sharber and Heikkila (1972) argue that the Fermi-mechanism is dominant in the acceleration of auroral electrons. Their conclusion is based on observations of what they call Λ events in data obtained onboard the satellite ISIS I in polar orbit. These events show an energy dependent pitch angle distribution such that the spectrum peaks at high energies (perhaps 10 kev) at pitch angles approaching zero, and is softer at higher pitch angles. Typically a hollow loss cone is evident resulting in a "topless Λ" event. The spatial extent of this Λ event is ∿ 100 km. From a morphological point of view, the Λ events probably coincide with the "inverted V" events discussed previously, again mainly because they also represent regions of widespread particle precipitation. It is suggested that the class (2) distribution of the electrons responsible for the widespread background aurora observed here and by Pazich (1973) may be caused by the operation of this mechanism on field lines which have collapsed to a more dipole-like configuration following the substorm activity preceding the rocket flights.

The Fermi-mechanism cannot by itself be responsible for the intense field-aligned intensities of the class (3) distributions observed in bright auroral arcs. The characteristic distributions have a relatively small spatial extent, i.e., the visible auroral arcs. Even if the arc is produced by some spatially uniform process, such as Fermi-betatron, acting on a strongly structured spatial distribution of particle density, this cannot account for the observed differences in energy and pitch angle distribution which occur over such small

spatial distances

Another apparent argument against the Fermi mechanism as being important in active situations is that velocity dispersion measurements during highly time-structured events observed by rockets usually indicate that the accelerating mechanism is acting relatively close to the ionosphere - certainly not in the equatorial plane (Evans, 1967). However, these observations do not rule out the possibility of the Fermi-betatron process acting in active situations but merely that the intensity may be further modulated by locally occurring mechanisms.

5.2 Parallel Electric Fields

The measurement of peaks in the spectra of precipitated electrons (McIlwain, 1960; Evans, 1968; and others) increased interest in the possibility that parallel electrostatic fields are responsible for at least part of the spectral character of the precipitated particles. Later, direct observations of field-aligned currents associated with auroral particle precipitation (Cloutier et al., 1970; Choy et al., 1971) provided the experimental impetus to an increase in theoretical consideration of the effects of field-aligned currents on the plasma contained in the same flux tubes, particularly with regard to the possibility that such currents are responsible for the formation of parallel electric fields.

5.2.1 The Modification of Particle Distributions by Parallel Electric Fields

Consider a flux tube of arbitrary cross section (Fig. 5.1), with a total potential difference V between points R and Q on the same field line such that the energy of an electron is increased and becomes (c.f. Roederer, 1970)

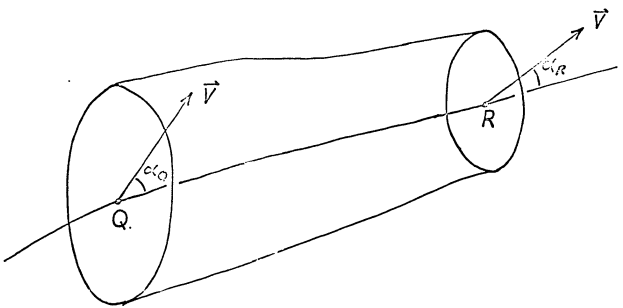

Fig. 5.1 Illustrating the geometry of a flux tube around a field line linking points R and Q.

$$E_R = E_Q + eV$$

For convenience write

$$E_R = aE_Q$$

where $a > 1$.

Assume that the magnitude of the magnetic field increases by a factor b, as would be the case for particles accelerated towards the ionosphere.

$$B_R = bB_Q$$

where $b > 1$.

From the conservation of magnetic moment

$$\frac{E_R \sin^2 \alpha_R}{B_R} = \frac{E_Q \sin^2 \alpha_Q}{B_Q}$$

Combining the last three equations yields

$$\sin \alpha_R = \left(\frac{b}{a}\right)^{\frac{1}{2}} \sin \alpha_Q \qquad (5.1)$$

For the electric and magnetic field configuration considered here, $\alpha_Q = 90^\circ$ is the maximum pitch angle available at Q to particles which

eventually reach R. Thus for $b < \alpha$, (5.1) shows that there exists a value of pitch angle (α) at R above which the distribution is zero. This cut-off value is given by

$$\sin \alpha_{\text{cut-off}} = \left(\frac{b}{a}\right)^{\frac{1}{2}}$$

It is not important that the electric field be uniform over the length of the flux tube. The important parameters are the total change in energy due to the two fields. To illustrate the relationship between the parameters involved, consider the case where R is the point of observation, and Q is the point on the field line above the observation point where the downcoming electrons enter the electric field region. Assuming the point of observation to be the rocket altitude, taken as 200 km, then for a given value of the parameter a, it is possible to locate a distance along the field line below which all the parallel acceleration must occur in order to produce a pitch angle cut-off at some given $\alpha_{\text{cut-off}} < 90^{\circ}$. The distance along the field line is simply that at which the magnetic field strength is reduced by a factor b from the value at the rocket altitude. Curves illustrating the relationship between these two parameters required to produce pitch angle cut-offs of 45° and 75° at the rocket altitude are shown in Fig. 5.2. The relationship between the parameter b and the distance along the field line were obtained from a field model calculation for a field line passing near Poker Flat and assuming a value of B = 52,000 γ at 200 km.

As an example, if the energy of the particles is increased by a

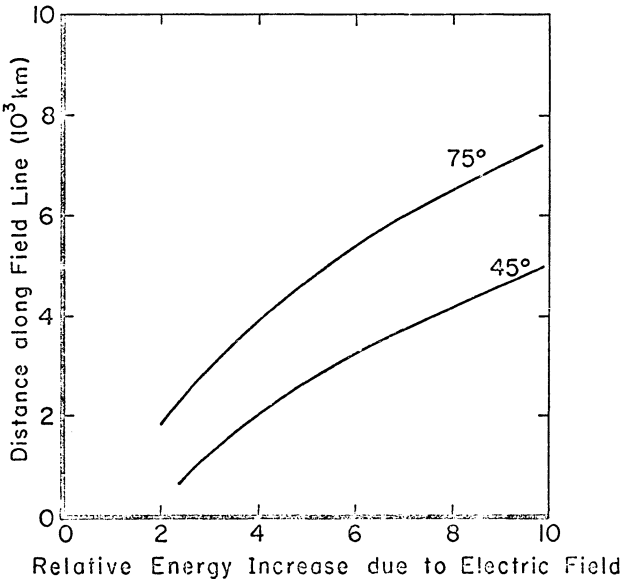

Fig. 5.2 The relationship between the energy increase produced by a parallel electric field, and distance along the field line within which it must occur to produce a pitch angle cut-off at 45° and 75°.

factor a = 5 by the action of a parallel electric field, then the curve shows that the acceleration has to occur below an altitude of 4,600 km to produce a cut-off at 75° or below 2,500 km to produce a cut-off at 45°.

The pitch angle distribution within the cut-off depends on the initial distribution for $0 < \alpha < 90^{\circ}$. Application of Liouville's theorem, which for this problem reduces to the statement

$$\frac{j(E, \alpha)}{E} = \text{const.}$$

along a particle trajectory, shows that an initial isotropic distribution will remain isotropic for $\alpha < \alpha_{\text{cut-off}}$ and will be zero for $\alpha > \alpha_{\text{cut-off}}$. Initial distributions other than isotropic will be modified in a more complicated way. However, for the production of a sharp cut-off, it is only necessary that the initial pitch angle distribution be smooth near 90°.

The observed pitch angle distribution will also be modified by backscattered electrons. In the energy range considered here ($\sim$ 10 kev) the upgoing intensity due to backscattering is typically seen to be $\sim$ 20% of the downgoing intensity (Pazich, 1973). Thus the atmospheric cut-off would show as a decrease in intensity by a factor of 5 near 90°. This is similar to several examples in this thesis. The backscattered distribution is isotropic over the range $90^{\circ} - 180^{\circ}$. In the case where the particles originally gained virtually all their energy from an electric potential drop, the upgoing particles will

be reflected from the electric field region, thus producing an isotropic background in the range 0^{o} - 90^{o}, with a magnitude $\sim$ 20% of the original downward intensity. Thus the cut-off due to the electric field would still show as a factor of $\sim$ 5 increase in intensity over this background.

It is estimated that the cut-off angle should not be larger than 75^{o} to be distinguishable from the atmospheric cut-off. Referring to the previous example, this value of 75^{o} implies that if no cut-off is observed, then the region of parallel electric field must extend beyond a distance of 4,600 km along the field line.

5.3 Evidence for the Existence of Parallel Electric Fields

Two main mechanisms which may produce parallel electric fields have been considered. They are the formation of electrostatic double layers (Langmiur, 1929; Carlqvist, 1972; Bloch, 1972), and anomalous resistance produced by current driven plasma turbulence along the field lines (Swift, 1965; Kindel and Kennel, 1971). In both cases, it is possible to derive the conditions for the onset of the instability leading to the potential drop. However, to account for the kv potentials required to produce the observed electron spectra requires that the solutions be extended to the non-linear limit, which has not been done analytically. The main evidence that such processes can produce potentials of the required magnitude are the laboratory observations of potential drops in gas discharges (Langmuir, 1929) and the production of 100 kv X-rays in a two stream plasma (Smullen and Getty, 1962).

Kindel and Kennel (1971) calculate the total potential drop across the region of anomalous resistance as perhaps 6 kv. This result has been lately widely discussed as the acceleration mechanism responsible

for the more energetic and field-aligned electron distributions (e.g., Berko, 1973). O'Brien (1970) and Sharber and Heikkila (1972) argue that parallel d.c. electric fields are not important in the energization of auroral particles. These authors note the observed simultaneous precipitation of protons and electrons, and point out that "an electrostatic field that simultaneously accelerated in the same direction particles with opposite polarities would be a remarkable one indeed". However, observations of precipitated protons usually exhibit a broad spectrum with most of the energy being carried by protons of energy greater than a few tens of kev (Romick and Sharp, 1967). These protons are relatively unaffected by parallel electrostatic potential drops of the magnitude calculated by Kindel and Kennel (1971).

Another fact to be considered is that the type of precipitated electron spectrum usually observed is not truly monoenergetic but shows a peak rising in intensity a factor of a few above an otherwise monotonically decreasing spectrum. Thus the total spectrum cannot be simply produced by an electric field acting on a source of zero-energy electrons. However, it may be possible to imagine ways in which a parallel electric field, together with other mechanisms, could produce the observed spectrum. Thus the overall spectrum cannot be produced simply by particles with initial energy near zero falling through a potential drop. However, one model which requires a unique electric potential distribution along the field line and a continuous injection of low energy particles over the whole field line length has been proposed. (Matthews and Pongratz, 1973). In their model the electric field region extends beyond 10 Re.

There is very little direct experimental evidence for the existence of parallel d.c. electric fields. Mozer and Bruston (1966a, b) interpret anticorrelations observed between precipitating energetic electrons (> 65 kev) and protons as evidence for the existence of a parallel field. Mozer and Fahleson (1970) show evidence for a field of $\sim$ 30 mv m^{-1}, directed downwards, i.e., so as to accelerate electrons upwards. Gurnett and Frank (1973) suggest that the observed difference between horizontal electric field magnitudes of INJUN 5 altitudes ($\sim$ 50 mv m^{-1} at 2400 km) and at rocket altitudes ($\sim$ 10 mv m^{-1} at 250 km) is evidence for the existence of parallel field, but as the data were taken during different events, the conclusion must be considered doubtful.

Gurnett (1972) calculates the line integral $\phi = \int \vec{E} \cdot \vec{ds}$ along the satellite trajectory through an "inverted V" event. Figure 5.3, a reproduction of his Figs. 9 and 10, illustrates the results, on the assumption that the electric potential lines close across the event region as shown. The line integral then yields the parallel potential drop below the satellite. In the case shown the result was Φ_s = 6 kv. The energy of the broad peak in the inverted V was $\sim$ 4 kev, hence there should be a peak at $\sim$ 10 kev in the precipitated electron spectrum as observed, at rocket altitudes. The fact that this acceleration is produced below the satellite can explain nicely the lack of true monoenergetic peaks in the electron spectra measured by Frank and Ackerson (1971), if these are, in fact, produced by parallel electric fields.

A parallel electric field acting on a uniform zero-energy col-

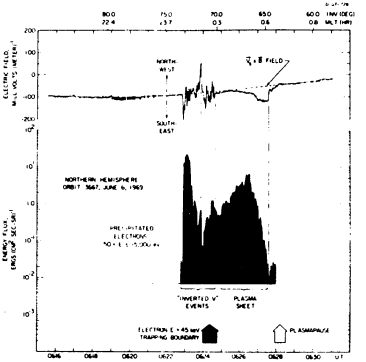

Figure 9

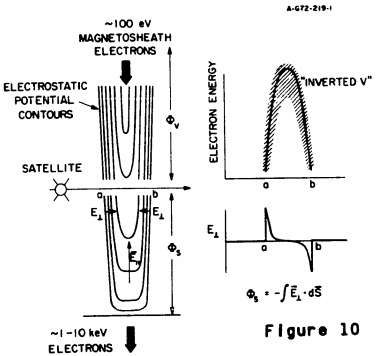

Figure 10

Fig. 5.3 Electric field measurements made as the polar-orbiting satellite INJUN 5 passed through an "inverted V" event. An idealized model of the electrostatic potential distribution inferred from the measurements is illustrated. (Gurnett, 1972)

lisionless plasma will produce a field-aligned monoenergetic particle distribution. However, when acting on a relatively energetic particle population, the resultant distribution is only field-aligned to the extent that there exists an upper cut-off in the pitch angle distribution (Section 5.2.1). Whalen and McDiarmid (1972) observed such a sharp cut-off in the distribution of 7.8 kev electrons measured in a bright auroral arc, one of several active arcs penetrated by a rocket. Their spectrum resolution is limited by the relatively long spin period ($\sim$ 2 sec), and a comparison with the data presented in this thesis is difficult. The distribution is unique in that the intensity decreases by a factor of $\sim$ 150 from 10^{o} to $\sim 50^{o}$, where there is a sharp change of slope and the intensity is constant over the pitch angle range 60^{o} - 140^{o}. This seems to be by far the best observation indicating the existence of local parallel potential drops contributing significantly to the energy of precipitating electrons.

In the data presented in this thesis, there is no evidence of a cutoff occurring at any pitch angle much less than 90^{o}. In the cases where a simple field-aligned intensity was observed, the pitch angle distribution showed the intensity monotonically decreasing with pitch angle over the entire range observed. This observation is similar to those of Pazich (1973).

The lack of a well-defined pitch angle cutoff implies that simple parallel electric potential drops at low altitudes are not the dominant mechanism in the acceleration of the electrons measured in the bright arcs described in this thesis.

If parallel electric fields act at greater altitudes, however,

the pitch angle cutoff produced may be outside the loss cone, and therefore will not be observed at rocket altitudes. Alternatively, conservation of magnetic moment, and perhaps pitch angle diffusion, will tend to repopulate the larger pitch angles before the particles reach rocket altitudes. In the cases where strongly field-aligned intensities were observed, there was still no well-defined cutoff. Thus, again, if parallel electric fields contributed significantly to the energy of the electrons observed in this study, the pitch angle distribution must have been further modified by processes occurring at altitudes lower than the region of the electric field.

It is concluded, therefore, that if parallel d.c. electric fields are important in the energization of auroral particles, measured in most rocket experiments, they occur at altitudes considerably greater than that of the topside ionosphere.

Scarf et al. (1973) have detected field-aligned currents at altitudes of a few earth radii. These currents were accompanied by intense VLF electrostatic waves, which may indicate the existence of turbulent resistivity produced by a current-driven instability at the boundary. This instability in turn, may produce a potential drop along the field line. A potential drop along the length of a field line at L = 1.24 has been inferred from observations of barium ions injected along the field line (Wescott et al., 1973).

It is possible that a pitch angle cutoff may occasionally exist near 90°. Records such as T = 295 (Fig. 3.18) possibly show some evidence for a cutoff at $\alpha \sim 80^{\circ}$. Using Eq. (5.3) this cutoff corresponds to a parallel potential drop of $\sim$ 300 V, similar to the value obtained

by Albert and Lindstrom (1970). However, a cutoff near 90^{o} will not be well resolved. The intensity decreases sharply anyway because of the effects of atmospheric interactions, which maximize at $\alpha = 90^{o}$ for any energy. At angles near 90^{o}, the effects are strongly energy-dependent, which may in itself explain the decrease in intensity for pitch angles $< 90^{o}$ in these data, as well as in the case described by Albert and Lindstrom (1970).

5.4 Acceleration by Wave-Particle Interactions

The observation by Whalen and McDiarmid (1972) of a strongly field-aligned spike superimposed on a hollow loss cone suggests that processes other than parallel electric fields described in the previous section are occurring. Following Whalen and McDiarmid, it is suggested that the electrons appearing in the center of a hollow loss cone distribution have been accelerated by some plasma instability and form a separate population from that of the remainder of the distribution. These events are closely associated in space with active bright auroras. Observations of VLF hiss strongly suggest that instability mechanisms are acting somewhere along the field lines on which are occurring bright, active auroras (Gurnett and Frank, 1972). Some rocket measurements even place the source of the hiss in the visible aurora between 90 and 110 km altitude (Ungstrup, 1971).

At first this explanation may seem unlikely due to the fact that these peculiar pitch angle distributions were observed in regions of relatively weak aurora, albeit close to active, bright forms where one might expect any turbulence to have the greatest amplitude. However, a close examination of individual pitch angle scans, such as

shown in Fig. 3.3, shows that at the higher intensities, there appears to be a "shoulder" on the field-aligned distribution. It appears that in this case the field-aligned component has such a magnitude that the higher pitch angle "wings" tend to fill up the hollow loss cone. Such shoulders are observed several times in the most intense regions. In the most intense events, the flat loss cone may be completely masked by the field-aligned component.

Such a strongly structured pitch angle distribution within the loss cone could not have been produced at the equatorial plane. This is because the region of the loss cone covered by the distribution maps to small fraction of a degree at the equator, and it is hard to imagine a process which can produce strong anisotropies over such a small pitch angle range.

For the same reason, strong anisotropies cannot be produced by Fermi acceleration. In addition, the Fermi process will not produce pitch angle characteristics which change over distances of $\sim$ 1 km, as is observed here. A local parallel electric field has already been ruled out.

It is concluded that the mechanism which best accounts for these peculiar pitch angle distribution is the acceleration of particles by plasma instabilities.

Several plasma instability mechanisms have been proposed to account for observations of energetic auroral particles.

Direct acceleration of electrons to high energies by electrostatic plasma oscillations was suggested by Perkins (1968) to explain the 10 Hz periodicity in precipitated electrons observed by Evans

(1967). The energy for the oscillations was derived from a two stream or "bump on the tail" instability, where the bump corresponds to the monoenergetic peak at a few kev in the electron spectra observed by Evans (1968) and others. This periodicity, explained by Perkins, is probably responsible for the production of flickering aurora (Beach et al., 1968). The observation of flickering in the bright, folded arc penetrated by payload 18.17, and the measurement of a strongly peaked electron spectrum in the same arc suggests that mechanisms such as described by Perkins (1968) were occurring.

Swift (1968; 1970) proposed a method of accelerating particles by electrostatic waves, specifically produced by a loss cone instability in the ring current protons. The waves propagate almost perpendicularly to the field lines and are capable of accelerating electrons along the field line. Johnstone (1971) interpreted rocket measurements of precipitating electron pulsations as a manifestation of this mechanism. This is probably the only attempt to date to identify a specific acceleration process by direct measurement.

In the theory of Kindel and Kennel (1971), electrostatic waves with propagation vector $\vec{k}$ nearly perpendicular to $\vec{B}$ are destabilized at a lower current than those with $\vec{k} \| \vec{B}$. It seems reasonable that the mechanism suggested by Swift (1970) may be effective in several types of unstable situations leading to the generation of electrostatic waves.

CHAPTER 6

SUMMARY AND MAIN CONCLUSIONS

Pitch angle distributions and three point energy spectra of precipitating electrons were measured by rocket-borne instruments in order to investigate the acceleration and precipitation mechanisms involved. The measurements were made in a region of relatively weak, diffuse aurora in which were brighter, more discrete arcs. The brightest arc ($\sim$ 20 kR in λ4278) contained a westward propagating fold which the rocket intercepted, thus effectively crossing the same arc three times. This auroral arc system was the westward extention of intense substorm activity which had been occurring for several hours prior to the launch of the rocket.

The analysis of the observations can conveniently be divided into two parts; the overall particle-aurora morphology, and the interpretation of the detailed structure of the electric distributions in terms of specific acceleration and precipitation mechanisms. In each of these categories, several conclusions have been reached, the more important of which are summarized here.

6.1 Particle-Aurora Morphology

(i) Relationship between electron precipitation and visible aurora

The delayed correspondence between variations in the 10 kev data from the two sections of the payload showed the variations to be spatial in origin. In addition, there was a close correspondence between these variations and variations in the visible aurora at the corresponding point in the trajectory. A threshold was apparent

for the production of a visible aurora as recorded by the all-sky cameras. As measured by the three fixed-energy detectors, this threshold is ~ 1.2 ergs cm^{-1} sec^{-1}. This, in turn, corresponds to an integrated vertical intensity of ~ 0.5 kR in $\lambda 4278$, (Dalgarno et al., 1965) which is in reasonable agreement with estimates of the threshold intensity required to produce an image in an all-sky photograph and which also corresponds approximately to the brightness classification IBC I. Above the threshold, a correspondence between more-or-less discrete auroral forms as recorded by all-sky photographs and features of the electric precipitation record was made.

(ii) Pitch angle distributions

There is also apparent a threshold in the precipitated energy for the occurrence of field-aligned anisotropies in the pitch angle distribution of the higher-energy electrons. This threshold corresponds approximately to that required to produce an IBC II aurora. There is one exceptional case in the data near T = 320. This case is caused by a very peculiar pitch angle distribution occurring at a relatively low intensity. It provides a clue to the mechanism involved in the acceleration and precipitation of the electrons.

In the diffuse aurora, the pitch angle distribution is mostly isotropic, sometimes showing a broad peak near 60°. This distribution is in agreement with the concept of precipitation produced by "weak" pitch angle diffusion (Kennel and Petschek, 1966).

It is concluded that, above this threshold, acceleration and precipitation mechanisms occur which further enhance the energy

and intensity of the precipitating electrons. These mechanisms tend to produce the observed field-aligned pitch angle distribution. Comparison with other observations suggests that such field-aligned intensities constitute a current parallel to the field lines. Theoretical treatments indicate that such currents can lead to several plasma instabilities in the topside ionosphere. The main ones considered to date are ion acoustic and ion cyclotron turbulence, and the Kelvin-Helmholtz instability due to the magnetic shear produced by a field-aligned sheet current. This last mechanism is considered a likely cause of the type of fold in the brightest auroral arc encountered by the rocket (Hallinan et al., 1972).

The field-aligned "burst" of 2.5 kev electrons observed immediately equatorward of the diffuse aurora appears to be a separate phenomenon. It probably corresponds to the field-aligned "bursts" of 2.3 kev electrons described by Berko (1973). The data obtained on this rocket flight do not provide any information on the source of these electrons, except that they do not appear to have been accelerated by a parellel electric field.

(iii) Energy spectra

Apart from the "burst" of 2.5 kev electrons at the equatorward edge of the diffuse aurora, the 3-point energy spectral data indicate that the electron spectrum peaks at an energy $\sim$ 5 kev over the whole region of diffuse aurora, rising to $\sim$ 10 kev in the brightest arc. The latter observation is consistent with most previous observations, but the former is not. The spectrum of electrons producing diffuse aurora is usually observed to decrease

smoothly towards higher energies. It is possible that the peaked spectrum observed in this case was produced by Fermi-acceleration on collapsing field lines following the strong substorm activity prior to the observation.

(iv) The bright, folded arc as a boundary

The bright, folded arc forms a boundary between regions characterized by a hard electron spectrum to the south, and a relatively soft spectrum to the north. In addition, the separation follows the form of the fold, implying that the visible fold maps a fold in the boundary between the two electron populations. The spectral differences are most marked close to the visible arc. Comparison with previous observations of similar arcs suggests that field-aligned currents occur at the boundary.

6.2 Acceleration and Precipitation Mechanisms

The data which provide the most information on acceleration and precipitation mechanisms are the pitch angle distributions, principally of the 10 kev electrons. While it is not possible to make a specific identification of a particular mechanism, the range of possibilities can be narrowed by specifically excluding some possible mechanisms.

(i) Parallel electric fields

Parallel electric fields have often been discussed as being responsible for the monoenergetic spectra and field-aligned pitch angle distributions of precipitating electrons often observed in bright auroral arcs. Velocity dispersion measurements usually indicate that the electrons are accelerated within $\sim$ 6000 km of

the ionosphere. This is the region in which theoretical considerations indicated that ion acoustic (Swift, 1968) or ion cyclotron (Kindel and Kennel, 1971) turbulence may produce a potential drop along field lines when a field-aligned current exceeds a critical value. However, if such a potential drop contributed a significant proportion of the particle energy, the pitch angle distribution would show a strong cutoff at some angle $< 90^{\circ}$. This is not observed in the data obtained on payload 18.17, nor is it usually observed. One reported observation (Whalen and McDiarmid, 1972) shows an apparently clear example of such a pitch angle cutoff. However, the pitch angle distributions observed on payload 18.17 show detailed structure which excludes the possibility that the pitch angle distribution produced by an electric field is subsequently modified by scattering

Thus is is concluded that low altitude parallel electric fields are not important in the energization of auroral particles.

Parallel electric fields may occur at greater altitudes. In this case, the pitch angle cutoff will be outside the loss cone observed at the rocket. In quiet aurora, there is not sufficient temporal structure to allow velocity dispersion measurements, so the possibility of acceleration by a distant electric field cannot be ruled out in this case.

(ii) Wave-particle mechanisms

The observation of strongly structured pitch angle distributions with a sharp peak at low pitch angles superimposed on an otherwise smooth distribution, sometimes with a broad peak near 60°, indicates that the sharply field-aligned particles were accelerated

by some wave-particle interaction. In particular, a mechanism such as proposed by Swift (1970) seems very plausible. In this mechanism, electrostatic waves, propagating nearly perpendicularly to the magnetic field accelerate electrons along the direction of the field line to velocities many times that of the wave phase velocity. The result is a nearly monoenergetic, strongly field-aligned intensity, as is commonly observed in bright auroral arcs.

(iii) Fermi mechanisms

The Fermi mechanism has often been invoked to account for both field-aligned intensities and monoenergetic spectra. The mechanism acts on particles through their bounce motion along field lines, and thus operates on a relatively large scale. It cannot account for the small scale variations in particle properties observed on rockets and by other means. It is possible that the Fermi mechanism is effective in the production of widespread, relatively uniform particle precipitation. The field-aligned nature of the intensity produced by the Fermi mechanism cannot be detected at rocket altitudes, because the pitch angle range observed there is only a small function of the distribution at the equatorial plane. However, the spectrum peaked at $\sim$ 5 kev observed in the diffuse aurora described in this thesis may be a manifestation of the Fermi mechanism operating on collapsing field lines produced by substorm activity.

6.3 Conclusion

A high degree of correspondence was found between variations in the characteristics of precipitated electrons and variations in the structure of the visible aurora. Further, it was found that

the results obtained from the analysis of the data obtained from the flight of payload 18.17 were consistent with the results of previous analyses. This overall consistency suggests that ground-based measurements of auroral phenomena may be used to directly infer some of the properties of the precipitating electrons.

Detailed examination of the energy and, more particularly, pitch angle distributions of the precipitating electrons shows that wave-particle interactions at low altitudes must be responsible for the intense field-aligned distributions measured in bright, active auroras. Simple parallel electric fields of the operation of the Fermi mechanism are specifically ruled out. However, either of these mechanisms may be responsible for the characteristics of the electrons measured in the widespread regions of diffuse aurora.

REFERENCES

Ackerson, K. L. and L. A. Frank, Correlated satellite measurements of low energy electron precipitation and ground-based observations of a visible auroral arc, J. Geophys. Res., 77, 1128, 1972

Akasofu, S.-I., Polar and Magnetospheric Substorms, D. Reidel Publ. Co., Dordrecht, Holland, 1968.

Akasofu, S.-I., S. Chapman and C.-I. Meng, The polar electrojet, J. Atmos. Terr. Phys., 27, 1275, 1965.

Albert, R. D. and P. J. Lindstrom, Auroral particle precipitation and trapping caused by electrostatic double layers in the ionosphere, Science, 170, 1398, 1970.

Axford, W. I., Magnetospheric convection, Rev. Geophys., I, (1,), 421, 1969.

Beach, R. F., G. R. Cresswell, T. N. Davis, T. J. Hallinan and L. R. Sweet, Flickering, a 10 Hz fluctuation within bright auroras, Planet. Space Sci., 16, 1525, 1968.

Berger, M. J., S. M. Seltzer and K. Maeda, Energy deposition by auroral electrons in the atmosphere, J. Atmos. Terr. Phys., 32, 1015, 1970.

Berko, F. W., Distributions and characteristics of high latitude field-aligned electron precipitation, J. Geophys. Res., 78, 1615, 1973.

Block, L. P., Potential double layers in the ionosphere, Cosmic Electrodynamics, 3, 349, 1972.

Boyd, J. S., A. E. Belon and G. J. Romick, Latitude and time variations in precipitated electron energy inferred from measurements of auroral heights, J. Geophys. Res., 76, 7694, 1971.

Brice, N., Bulk motion of the magnetosphere, J. Geophys. Res., 72, 5193, 1967.

Bryant, D. A., G. M. Courtier and G. Bennett, Electron intensities over two auroral arcs, Planet. Space Sci., 21, 165, 1973.

Carlqvist, P., On the formation of double layers in plasmas, Cosmic Electrodynamics, 3, 377, 1972.

Carpenter, D. L., Whistler studies of the plasmapause in the magnetosphere, 1, Temporal variations in the position of the knee and some evidence on plasma motions near the knee, J. Geophys. Res., 71, 693, 1966.

Carpenter, D. L., K. Stone, J. C. Siren and T. L. Crystal, Magnetospheric electric fields deduced from drifting whistler paths, J. Geophys. Res., 77, 2819, 1972.

Chappell, C. R., K. K. Harris and G. W. Sharp, OGO 5 measurements of the plasmapause during observations of SAR arcs, J. Geophys. Res., 76, 2357, 1971.

Chase, L. M., Evidence that the plasma sheet is the source of auroral electrons, J. Geophys. Res., 74, 348, 1969.

Choy, W., R. L. Arnoldy, W. Potter, P. Kintner and L. J. Cahill, Field-aligned particle currents near an auroral arc, J. Geophys. Res., 76, 8279, 1971.

Cloutier, P. A., H. R. Anderson, R. J. Park, R. R. Vondrak, R. J. Spiger and B. R. Sandel, Detection of geomagnetically aligned currents associated with an auroral arc, J. Geophys. Res., 75, 2595, 1970.

Cornwall, J. M., F. V. Coroniti and R. M. Thorne, Turbulent loss of ring current protons, J. Geophys. Res., 75, 4699, 1970.

Cornwall, J. M.. F. V. Coroniti and R. M. Thorne, Unified theory of SAR arc formation at the plasmapause, J. Geophys. Res., 76, 4428, 1971.

Dalgarno, A., I. D. Latimer and J. W. McConkey, Corpuscular bombardment and N_2^+ radiation, Planet. Space Sci., 13, 1008, 1965.

Davis, T. N. and R. Parthasarathy, The relationship between polar magnetic activity DP and growth of the geomagnetic ring current, J. Geophys. Res., 72, 5825, 1967.

Davis, T. N., Temporal behavior of energy injection into the geomagnetic ring current, J. Geophys. Res., 74, 6266, 1969.

Eather, R. H. and R. L. Carovillano, The ring current as the source region for proton auroras, Cosmic Electrodynamics, 2, 105, 1971.

Evans, D. S., A 10 cps periodicity in the precipitation of auroral zone electrons, J. Geophys. Res., 72, 4281, 1967.

Evans, D. S., The observations of a near monoenergetic flux of auroral electrons, J. Geophys. Res., 73, 2315, 1968.

Frank, L. A., Direct detection of asymmetric increases of extraterrestrial 'ring current' proton intensities in the outer radiation zone, J. Geophys. Res., 75, 1263, 1970.

Frank, L. A., Relationship of the plasma sheet, ring current, trapping boundary and plasmapause near the magnetic equator and local midnight, J. Geophys. Res., 76, 2265, 1971.

Frank, L. A. and H. C. Owens, Omnidirectional intensity contours of low-energy protons ($0.5 \leq E \leq 50$ kev) in the earth's outer radiation zone at the magnetic equator, J. Geophys. Res., 75, 1269, 1970.

Frank, L. A. and K. L. Ackerson, Observations of charged particle precipitation into the auroral zone, J. Geophys. Res., 76, 3612, 1971.

Gurnett, D. A., Electric field and plasma observations in the magnetosphere, paper presented at COSPAR, IAGA, URSI Symposium, Madrid, Spain, May 1972.

Gurnett, D. A. and L. A. Frank, VLF hiss and related plasma observations in the polar magnetosphere, J. Geophys. Res., 77, 12, 1972.

Gurnett, D. A. and L. A. Frank, Observed relationship between electric fields and auroral particle precipitation, J. Geophys. Res., 78, 145, 1973.

Hallinan, T. J., T. N. Davis and H. F. Webster, Auroral spirals: A consequence of field-aligned currents, Geophysical Inst. Rept. UAG R-221, Fairbanks, Alaska, 1972.

Hasagawa, A., Plasma instabilities in the magnetosphere, Rev. Geophys. and Space Sci., 9, 703, 1971.

Hoch, R. J., C. R. Batishko and K. C. Clark, Simultaneous spectrographic triangulation of an SAR arc and a hydrogen arc, J. Geophys. Res., 76, 6185, 1971.

Hones, E. W., R. H. Karas, L. J. Lanzerotti and S.-I. Akasofu, Magnetospheric substorms on September 14, 1968, J. Geophys. Res., 76, 6765, 1971a.

Hones, E. W., J. R. Ashbridge, S. J. Bame and S. Singer, Energy spectra and angular distributions of particles in the plasma sheet and their comparison with rocket measurements over the auroral zone, J. Geophys. Res., 76, 63, 1971b.

Johnstone, A. D., Measurements of low energy protons in a pulsating aurora, Ph.D. Thesis, University of Alaska, Fairbanks, Alaska, 1970.

Johnstone, A. D., Correlation between electron and proton fluxes in postbreakup aurora, J. Geophys. Res., 76, 5259, 1971.

Johnstone, A. D., J. S. Boyd and T. N. Davis, A study of a small auroral substorm, (submitted to J. Geophys. Res.), 1973.

Johnstone, A. D. and T. N. Davis, Low altitude acceleration of auroral electrons observed by a mother-daughter rocket, (submitted to J. Geophys. Res.), 1973.

Kamiyama, H., Ionization and excitation by precipitating electrons, Rept. of Ionos. Space Res. Japan,, 20, 171, 1966.

Kennel, C. F. and H. E. Petschek, Limit of stably trapped particle fluxes, J. Geophys. Res., 71, 1, 1966.

Kindel, J. M. and C. F. Kennel, Topside current instabilities, J. Geophys. Res., 76, 3055, 1971.

Langmuir, I., The interaction of electron and positive ion space charges in cathode sheaths, Phys. Rev., 33, 954, 1929.

Marion, J. B., Classical Dynamics of Particles and Systems, Academic Press, New York, 1970.

Matthews, D. L. and M. C. Pongratz, What if $E_{\parallel} \neq 0$? A quantitative interpretation of observed auroral electron distributions, EOS, Trans. A.G.U., 54, 434, 1973.

McCormac, B. M., (Ed.), Radiation trapped in the earth's magnetic field; Proc. of Advanced Study Institute, Bergen, Norway, 1966.

McIlwain, C. E., Direct measurement of particles producing visible auroras, J. Geophys. Res., 65, 2727, 1960.

Montbriand, L. E., The proton aurora and auroral substorm, in The Radiating Atmosphere, B. M. McCormac (Ed.), D. Reidel Publ. Co., Dordrecht, Holland, 366, 1971.

Mozer, F. S. and P. Bruston, Properties of the auroral zone electron source deduced from electron spectrms and angular distributions, J. Geophys. Res., 71, 4451, 1966a.

Mozer, F. S. and P. Bruston, Auroral zone proton-electron anticorrelation, proton angular distributions, and electric fields, J. Geophys. Res., 71, 4461, 1966b.

Mozer, F. S. and U. V. Fahleson, Parallel and perpendicular electric fields in an aurora, Planet. Space Sci., 18, 1563, 1970.

Ness, N. F., The geomagnetic tail, Rev. Geophys., 7, 97, 1969.

O'Brien, B. J., A large diurnal variation of the geomagnetically trapped radiation, J. Geophys. Res., 68, 989, 1963.

O'Brien, B. J., Observations that a source of auroral energetic particles is not a parallel electric field, Planet. Space Sci., 18, 1821, 1970.

Owens, H. D. and L. A. Frank, Electron omnidirectional intensity contours in the earth's outer radiation zone at the magnetic equator, J. Geophys. Res., 73, 199, 1968.

Park, R. J. and P. A. Cloutier, Rocket-based measurements of Birkeland currents related to an auroral arc and electrojet, J. Geophys. Res., 76, 7714, 1971.

Pazich, P. M., Rocket-based measurements of auroral particle fluxes associated with field-aligned currents, Ph.D. Thesis, Rice University, Houston, Texas, 1973.

Perkins, F. W., Plasma-wave instabilities in the ionosphere over the aurora, J. Geophys. Res., 73, 6631, 1968.

Rearwin, S., Rocket measurements of low energy auroral electrons, J. Geophys. Res., 76, 4505, 1971.

Rees, M. H., Auroral ionization and excitation by incident auroral electrons, Planet. Space Sci., 11, 1209, 1963.

Rees, M. H., Note on the penetration of energetic electrons into the earth's atmosphere, Planet. Space Sci., 12, 722, 1964.

Rees, M. H., A. E. Belon and G. J. Romick, The systematic behavior of hydrogen emission in the aurora, Planet. Space Sci., 5, 87, 1961.

Roederer, J. G., Dynamics of Geomagnetically Trapped Radiation, Springer-Verlag, New York, 1970.

Romick, G. J. and R. D. Sharp, Simultaneous measurements of an incident hydrogen flux and the resulting hydrogen Balmer alpha emission in an auroral hydrogen arc. J. Geophys. Res., 72, 4791, 1967.

Russell, C. T. and R. M. Thorne, On the structure of the inner magnetosphere, Cosmic Electrodynamics, 1, 67, 1970.

Scarf, F. L., R. W. Fredericks, C. T. Russell, M. Kivelson, M. Neugebauer and C. R. Chappell, Observation of a current driven plasma instability at the outer zone plasma sheet boundary, J. Geophys. Res., 78, 2150, 1973.

Schield, M. A., and L. A. Frank, Electron observations between the inner edge of the plasma sheet and the plasmasphere, J. Geophys. Res., 75, 5401, 1970.

Sharber, J. R. and W. J. Heikkila, Fermi acceleration of auroral particles, J. Geophys. Res., 77, 3397, 1972.

Smullen, L. D. and W. D. Getty, Generation of a hot, dense plasma by a collective beam plasma interaction, Phys. Rev. Letters, 9, 3, 1962.

Stolarski, R. S., Calculation of auroral emission rates and heating effects, Planet. Space Sci., 16, 1265, 1968.

Stringer, W. J. and A. E. Belon, The morphology of the IQSY auroral oval, 1, interpretation of isoauroral diagrams, J. Geophys. Res., 72, 4415, 1967.

Swift, D. W., A mechanism for energizing electrons in the magnetosphere, J. Geophys. Res., 70, 3061, 1965.

Swift, D. W., Possible consequences of the asymmetric development of the ring current belt, Planet. Space Sci., 15, 835, 1967.

Swift, D. W., A new interpretation for VLF chorus, J. Geophys. Res., 73, 7447, 1968.

Swift, D. W., Particle acceleration by electrostatic waves, J. Geophys. Res., 75, 6324, 1970.

Taylor, H. E. and E. W. Hones, Adiabatic motion of auroral particles in a model of the electric and magnetic fields surrounding the earth, J. Geophys. Res., 70, 3605, 1965.

Ungstrup, E., Rocket observations of VLF hiss in aurora, Planet. Space Sci., 19, 1475, 1971.

Van Allen, J. A., C. E. McIlwain and G. H. Ludwig, Radiation observations with satellite 1958 e, J. Geophys. Res., 64, 271, 1959.

Vasyliunus, V. M., A survey of low-energy electrons in the evening sector of the magnetosphere with OGO 1 and OGO 3, J. Geophys. Res., 73, 2839, 1968.

Westerlund, L. H., The auroral electron energy spectrum extended to 45 ev, J. Geophys. Res., 74, 351, 1969.

Wescott, E. M., H. M. Peek, H. C. S. Nielsen, W. B. Murcray, R. J. Jensen and T. N. Davis, Two successful geomagnetic field-line tracing experiments. J. Geophys. Res., 77, 2982, 1972.

Whalen, B. A. and I. M. McDiarmid, Observations of magnetic field-aligned auroral electron precipitation, J. Geophys. Res., 77, 191, 1972.